Condensate-mediated reactivation of mumps virus infection under stress

Xiaojie Zhang[1], Sindhuja Sridharan[2], Ievgeniia Zagoriy[1], Christina Eugster Oegema[3], Cyan Ching[1,4], Tim Pflaesterer[1,5], Herman K. H. Fung[1], Ina Poser[3,6], Christoph W. Müller[1], Anthony A. Hyman[3], Mikhail M. Savitski[2,7] & Julia Mahamid[1,7]

1. Structural and Computational Biology Unit, European Molecular Biology Laboratory (EMBL), Meyerhofstraße 1, 69117, Heidelberg, Germany
2. Genome Biology Unit, European Molecular Biology Laboratory, Meyerhofstraße 1, 69117, Heidelberg, Germany
3. Max Planck Institute of Molecular Cell Biology and Genetics, Pfotenhauerstraße 108, 01307, Dresden, Germany
4. Current address: Molecular Biosciences, Centre for Molecular Biology, Heidelberg University, Im Neuenheimer Feld 282, 69120, Heidelberg, Germany
5. Current address: Institute of Pharmacy and Molecular Biotechnology, Heidelberg University, Im Neuenheimer Feld 364, 69120, Heidelberg, Germany
6. Current address: Dewpoint Therapeutics GmbH, Tatzberg 47, 01307, Dresden, Germany
7. Correspondence: mikhail.savitski@embl.de; julia.mahamid@embl.de

Summary

Viruses can establish both acute and persistent chronic infections, and some viruses have developed the ability to switch between the two. However, the molecular mechanisms that trigger a transition from a benign chronic infection into pathogenesis remain unknown. Here we investigated the role of the cellular stress response in provoking a chronic-to-acute transition in viral replication in a model of mumps virus infection. Using a combination of cell biology, whole-cell proteomics and cryo-electron tomography we show that stress induces phosphorylation of the disordered viral Phosphoprotein, which we suggest facilitates partitioning of the viral polymerase into preformed viral condensates, constituting the core components of the viral replication machinery. This occurs concomitantly with a conformational change in the viral nucleocapsids that exposes the viral genome and can further facilitate its replication. These changes in the viral condensate upon exogenous stress, accompanied by down-regulation of the host antiviral response, provide an environment that supports up-regulation of viral replication and virion release. Thus, we elucidate molecular and structural mechanisms of a stress-mediated switch that disrupts the equilibrium between the virome and the host in chronic infection.

Main text

The *Paramyxoviridae* family includes some of the most pathogenic viruses, such as measles (MeV) and mumps (MuV). Their acute intracellular replication following cell entry elicits a cellular stress response and the formation of stress granules as part of the host antiviral defense[1,2]. Viruses have thus evolved strategies to interfere with or exploit the stress response to facilitate their own replication[3,4]. These viruses can also establish chronic infection, wherein the host response and viral replication are balanced in a metastable equilibrium[5,6]. In the chronic state, viral replication and release are maintained at low levels, a mechanism proposed to contribute to lifelong immunity following natural infection or vaccination[7,8]. Chronic benign infection can, however, transition into severe diseases[9,10]. Yet, the molecular mechanisms that cause this transition remain largely unknown.

The established role of the cellular stress response in the acute state of viral infection[1,2] prompted us to investigate external stress as a potential trigger that disrupts the fine host-virus balance in chronic infection (Supplementary Discussion). We therefore established a persistent MuV infection by infecting a HeLa cell line with the MuV Enders strain (Methods, Supplementary Data 1). The cell line additionally expresses the stress granule protein mCherry-G3BP1 (Ras GTPase-activating protein-binding protein 1) as a marker of cellular stress[11].

MuV replication factories are cytoplasmic condensates that coarsen under stress

The negative single-stranded RNA genome of MuV contains seven transcription units encoding the proteins: nucleocapsid (N), viral/phospho- (V/P, co-transcriptional products), matrix (M), fusion (F), small hydrophobic (SH), hemagglutinin-neuraminidase (HN) and large (L) proteins. N protein self-assembles into a helical capsid that accommodates the MuV RNA genome on its surface to form a nucleocapsid, which serves to protect the viral genome and a template for viral replication. Viral genome transcription and replication are carried out by the viral RNA-dependent RNA polymerase (L) and require the phosphoprotein (P) that links between the nucleocapsid and the polymerase[12]. MuV transcription and replication requiring N, P and L take place at cytoplasmic viral factories[13]. The remaining MuV proteins are associated with nucleocapsid attachment to the inner side of the plasma membrane (HN), viral assembly (M), viral budding (F) and immunomodulation (V), respectively.

In our MuV infection culture model, cell division was maintained at normal levels (Extended Data Fig. 1a), similar to previously reported persistent infection models[7]. Cytoplasmic viral factories were detected using antibody staining against the N protein and imaged by confocal light microscopy. The cells did not contain stress granules (Extended Data Fig. 1a), while virions released into the medium were capable of infecting naive cells (Extended Data Fig. 1b), thus bearing hallmarks of a chronic benign infection[5].

We monitored how the MuV factories change under cellular stress. Both severe heat shock (1 h) and oxidative stress (by arsenate As(V) or arsenite As(III) up to 24 h) elicited stress granules[11], and resulted in an increase in viral factory size, concurrently with a decrease in their numbers (Fig. 1a-c, Extended Data Fig. 1c-l). This is reminiscent of coarsening behavior in liquid-like biomolecular condensates, which is driven by fusion[14] or Ostwald ripening[15], whereby larger droplets grow at the expense of smaller ones. Indeed, formation of liquid-like condensates by phase separation has been implicated in the replication and assembly of MeV and human respiratory syncytial virus during acute infection[16-18], as well as genome packaging of SARS-CoV-2[19,20] (Supplementary Discussion). Liquid-like condensates are often sensitive to hexanediol[21]. Hexanediol treatment that leads to dissolution of the liquid-like stress granules[11] also dissolved the viral factories to a large extent (40-60% in Fig. 1d, Extended Data Fig. 2a-c). This suggests that MuV factories are also liquid-like compartments.

To understand the basis for viral factory condensation, we expressed N and P, which we found to be highly transcribed in our chronic infection model (Extended Data Fig. 2d), in naive cells. Multivalent interactions mediated by intrinsically disordered regions (IDR) of proteins are often the driving force for condensate formation[16,22]. Both N and P contain disordered regions (Extended Data Fig. 2e) and can multimerise[23,24]. P-only transfection resulted in the formation of spherical cytoplasmic inclusions. N-only transfection resulted in small puncta throughout the cytoplasm. Co-transfection of N with P led to co-condensation into granules of comparable size to large viral factories (Fig. 1e, Extended Data Fig. 2f). Thus, condensation of MuV factories can be mediated by its highly disordered P protein. Combined, these results show that MuV viral factories form liquid-like condensates in chronic infection that change their behavior and coarsen under stress.

Stress alters phosphorylation and partitioning of viral proteins

We questioned whether the viral protein constituents in MuV factories are altered under stress in terms of protein abundance, post-translational modifications, and interactions. Whole-cell quantitative mass spectrometry (MS)[25] showed that non-stressed cells expressed high levels of MuV proteins (Extended Data Fig. 3a), and showed little change under all examined stress conditions (Methods, Extended Data Fig. 3b, Supplementary Data 2). Despite the stable total level of P, phosphopeptides spanning residues 292-328 (either S292, S294, T298 or S301) within its disordered region were elevated during stress (up to 6-fold in Fig. 1f, Supplementary Data 3). The elevated phosphorylation of P by host factors under stress may affect its phase behaviour[16] (Supplementary Discussion). Mapping the phosphorylation sites of P onto the recently reported structure of viral P-L polymerase complex from the closely-related parainfluenza virus 5[26] showed that the phosphorylation sites localize at the P-L interface (Fig. 1g). Due to complementary charges at the interaction interface on L, P phosphorylation is expected to stabilize its interaction with L.

We also found that P's co-transcriptional product V is phosphorylated on its zinc finger domain (S175 and S194) upon stress (Extended Data Fig. 3c). V is known to block the host antiviral response via interaction with the signal transducer and activator of transcription 1 (STAT1)[27,28] or STAT2[29]. Phosphorylation at S194 of V, predicted to localize near their interaction interface based on a homolog model of simian virus 5 V protein[30], suggests a stress-tunable role for V in suppressing host antiviral pathways. Thus, increased phosphorylation of the IDR-containing P and V could modulate the strength of interaction networks of both viral and host proteins.

The predicted stabilization of protein-protein interactions following phosphorylation may lead to either increased partitioning of proteins into the viral condensates or to formation of higher-order complexes. Both outcomes can be probed by assessing protein solubility using a lysate pelleting assay coupled with quantitative MS[25]. In solubility profiling, measuring the relative proportions of all cellular proteins in the "soluble" versus "insoluble" fractions can be used as a proxy for measuring the extent to which a protein partitions into condensates[25,31]. Such profiling revealed that significant proportions of the viral proteins N (~90%), M (~50-60%) and P (~60-70%) reside in the insoluble fraction in unstressed cells (Extended Data Fig. 3d,e). This is consistent with observations that N and M assemble into structured polymers[32], while P phase separates (Fig. 1e). All other viral proteins were predominantly soluble in unstressed cells, suggesting weak or transient interactions with the core factory proteins N and P[33].

Under stress, N, M and P proteins did not change solubility. However, L and V exhibited significant decrease in solubility, especially at more severe stress conditions (Fig. 1h, Extended Data Fig. 3e; Supplementary Data 4). Such changes suggest increased partitioning of L and V into viral condensates, which may be due to stronger interaction with core factory proteins[34] (Fig. 1g). Indeed, previous studies on MuV showed that L is enriched in viral factories during acute infection[33].

Taken together, proteomics analysis suggests modulation of the protein interaction network in the viral condensates during stress, which is likely facilitated through phosphorylation of P and V.

Stress induces a conformational switch in viral nucleocapsids

To visualize the structural change in the interaction networks suggested by the proteomics data, we performed cryo-electron tomography (ET) on the intracellular viral factories. MuV factories frequently localized in close proximity to stress granules (Fig. 1a). We therefore exploited the mCherry-G3BP1 fluorescence to perform 3D targeted cryo-focused ion beam (FIB) thinning and to locate unlabeled viral factories for cryo-ET (Methods, Extended Data Fig. 4a, Fig. 2a). At 1 h of 0.5 mM As(III) stress, filamentous structures resembling previously reported low resolution maps of MuV nucleocapsids[12,35] were seen in viral factories as entangled clusters (Fig. 2b), or near the plasma membrane and inside virions (Extended Data Fig. 4b). The data revealed 21-nm-diameter curved hollow filaments, consisting of repetitive units spaced ~5.5 nm along the filament axis (Fig. 2b). Tracing of the nucleocapsids

allowed quantitative analysis of changes in molecular crowding along the stress course (Fig. 2c-e, Extended Data Fig. 4c, Supplementary Movie 1-3). Nucleocapsid volume fractions in the viral condensates tripled from the control to 6 h of mild stress (30 µM As(III), Fig. 2e). In addition to the nucleocapsids, thin flexible densities extending from the nucleocapsids were abundant under stress conditions (Fig. 2d), potentially marking interaction partners of N. Strikingly, prolonged stress led to a morphological transition from curved to straight nucleocapsids (Fig. 2d,e, Extended Data Fig. 4c,d). The straight rigid appearance of the nucleocapsids is reminiscent of aberrant cytoplasmic MuV inclusions observed in tissue biopsies from patients suffering from myositis[10].

To interpret the morphological changes in the nucleocapsids under stress, we obtained a structure of the authentic MuV nucleocapsid. Nucleocapsids were isolated from stressed cells after 1 h of 0.5 mM As(III) (Extended Data Fig. 5a). Sucrose gradient fractionation coupled with negative staining electron microscopy (EM) and quantitative MS confirmed that the enriched filaments are MuV nucleocapsids (Extended Data Fig. 5b,c, Supplementary Data 5). The isolated nucleocapsids were curved, similar to their intracellular morphology at early timepoints of stress, but straightened upon addition of the RNA-mimicking molecule heparin (Extended Data Fig. 5d). This change in morphology was similar to the change in nucleocapsid morphology seen inside cells at prolonged stress conditions, suggesting that RNA engagement with the nucleocapsid may contribute to the change from curved to straight conformation.

We obtained two maps from subtomogram averaging on the heparin-straightened nucleocapsids at 1 h stress (Extended Data Figs. 5e,f, 6). The two maps exhibited different helical parameters (Fig. 3a): a 5.58 nm long-pitch structure constituting the majority class (77.7%) was resolved to 4.5 Å, and a 4.70 nm short-pitch class (21.3%) was resolved to 6.3 Å (Extended Data Fig. 6b,c, Extended Data Table 1). The most flexible C-terminal IDR of N (144 amino acids) was not resolved in either maps. We built an atomic model of the N protein into the majority class based on a homolog structure from parainfluenza virus 5 nucleoprotein (PDB: 4XJN, Extended Data Fig. 6d, Extended Data Table 1, Supplementary Movie 4). The model showed that the viral RNA genome is accommodated at the nucleocapsid outer surface, within a groove connecting the N-terminal domain (NTD) with the C-terminal domain (CTD) of the N protein (Fig. 3b,c, Extended Data Fig. 6e). Interactions between subunits in consecutive turns of the nucleocapsid are mediated by the CTD-arm helix (a region succeeding the CTD) which inserts between the NTDs of two subunits in the upper turn (Fig. 3d). Within the same turn, domain swapping between the NTD-arms (a region preceding the NTD) and CTD-arms of consecutive subunits formed extensive contacts at the nucleocapsid lumen (Fig. 3d). Density of this critical CTD-arm was missing in the map of the minority class indicating its higher flexibility (Fig. 3e), as only full-length protein was detected by western blot analysis (Extended Data Fig. 5g). Interestingly, both structural classes existed within the same nucleocapsid (Extended Data Fig. 6f), confirming previous studies on MeV and MuV nucleocapsids[36,37] that lead to a hypothesis of a regulatory role of the C-terminus of N in transcription

and replication of *paramyxoviridae*[38,39]. Indeed, tighter packing of subunits in the minority class resulted in an 8.4 Å shift of a loop in the upper subunits towards the lower subunits, resulting in less surface-exposed RNA binding pocket (Fig. 3f). The tighter packing also restricted the space available for the flexible C-terminal IDR to extend to the nucleocapsid surface (Fig. 3f, Extended Data Fig. 6f).

The two maps reflect the structural plasticity of N[12,35,37,40] (Supplementary Discussion), which has been previously suggested to contribute to different functional outcomes: protection of the viral genome from the host defense versus genome accessibility to promote viral replication. The tighter nucleocapsid structure of the minority class would protect the RNA from the host antiviral response, or may constitute a compacted state ready for virion assembly and release. On the other hand, the structure for the majority class under stress exhibits higher exposure of the RNA on the nucleocapsid surface and higher likelihood for the C-terminal IDR of N protein to interact with partner proteins, P and L at the nucleocapsid surface. Both factors would contribute to a conformation that can support viral replication.

With the structural models at hand, we examined the nucleocapsids in the cellular context. Their high curvature at early time points of stress provided maps at ~30 Å only, showing class averages of mixed helical rises (Extended Data Fig. 7a-c), in line with non-uniform conformations observed in the isolated nucleocapsids at the same stress timepoint. An in-cell map of straightened nucleocapsids at prolonged stress was resolved to 6.5 Å (30 µM As(III) or 1 mM As(V) for 6 h, Extended Data Fig. 7d-f). A single class was obtained that resembled the loose-packing majority structure of the isolated nucleocapsids, with clear luminal density for the CTD-arm and surface exposure of the RNA (Fig. 3g). However, additional densities at the nucleocapsid surface were exclusively found in the in-cell map (Fig. 3h). This region was previously suggested to form the interaction interface between N and P, mediated by their C-termini[12,41]. We speculate that the additional density in the in-cell map could therefore be the C-terminal IDR of N that becomes rigid due to its interaction with P under the prolonged stress conditions, consistent with our observation of abundant flexible densities near the nucleocapsids in the cellular tomograms (Fig. 2d, right). Thus, in cells under prolonged stress, the nucleocapsids adopt a homogenous conformation with a surface exposed viral genome that is likely to be more accessible for efficient transcription and replication by L.

Viral replication and release are accelerated by stress

We next addressed whether the stress-induced changes in viral protein modifications, their interactions and the nucleocapsid conformations have functional consequences for viral replication. We show that cellular stress led to a 2-3-fold increase in viral replication. Specifically, transcription levels as indicated by P/V and F genes showed steady increase over 24 h under 30 uM As(III), while that of N decreased after 6 h (Fig. 4a, Extended Data Fig. 8a), in agreement with previous reports on an autoregulatory behavior of N[42]. Viral replication, inferred from the genomic RNA level, was up-regulated at prolonged mild stress (Fig. 4a, Extended Data Fig. 8a, Supplementary Discussion). More severe stress by 1 mM

As(V) boosted both transcription and replication within 3 h (Fig. 4b, Extended Data Fig. 8b). Thus, the increase in the viral activity correlates with the severity of cellular stress.

Next, we measured N protein levels in the media as a proxy for the amount of viral particles released. The levels of both groups oscillated over 24 h, suggesting that the level of released virions is under regulation by host factors as shown for hepatitis C virus[3]. However, stress accelerated viral budding by 1.7-fold at 6 h, compared to that of the non-stressed cells (Fig. 4c and Extended Data Fig. 8c).

The increase in viral replication and release coincided with changes in host immune response. Using quantitative proteome analysis of host proteins, we identified a predominant down-regulation (88%) and a modest up-regulation (11%) of host proteins over the stress time course of 24 h (Extended Data Fig. 8d). While attenuation of the host antiviral defense by degradation of STAT1 has been documented in persistent infection[28], we found significant further down-regulation of type I interferon signaling pathway proteins, including the interferon signaling mediators (Janus kinase 1 and STAT2) and antiviral RNA binding proteins from the first hour of stress (Extended Data Fig. 8e). Down-regulation of STAT2 could in part be attributed to immunomodulation by V protein potentially facilitated by its phosphorylation (Extended Data Fig. 3c) at the interaction interface between the two proteins[29] (Supplementary Discussion).

Cellular stress therefore triggered increased viral transcription, replication, and facilitated viral release in in our chronic MuV infection model, along with the orchestrated down-regulation of the host antiviral response.

Conclusions

Our integrated study of MuV as a model system of chronic infection suggests a mechanistic model in which basal level of viral replication and budding is upregulated upon stress (Fig. 4d). During chronic infection, small viral factories consisting mainly of N and P proteins mediate slow replication of the virus. Stress triggers posttranslational modification of P by host factors that we suggest increases the interaction strength with L polymerase and promotes its partitioning into the viral factories. This is accompanied by a change in the liquid-like dynamics of the viral factories, as demonstrated by their coarsening. We postulate that the structural change in the N protein-based nucleocapsid seen under stress conditions allows the RNA to become more accessible to the L polymerase, thus facilitating higher levels of viral replication.

Taken together, our work demonstrates how a combination of whole-cell proteomics and cryo-ET provides a powerful tool to probe virus replication in the context of biomolecular condensates inside cells. Relatively modest changes in the phosphorylation state of the P protein and a small structural change in the nucleocapsid seem sufficient to disturb the delicate balance between the virus and host

cell during chronic infection. While the exact sequence of molecular events leading to the changes in the nucleocapsid structure under stress remains to be elucidated, future work, using genetics and in vitro reconstitution, should allow a full understanding of the mechanisms by which chronic infection is reactivated. It is tempting to speculate that such molecular switches induced following stress may have broad implications across a diverse family of viruses that establish chronic infection in the human host, and the diseases they elicit.

Acknowledgements

We thank EMBL core facilities, including the EMCF, ALMF, Genecore for access to instrumentation, microscopes, and assistance with data analysis, central IT and especially Thomas Hoffman for computational assistance. We thank Wim Hagen, Felix Weis, and the EMBL cryo-EM platform for access to EM microscopes and assistance in data acquisition. We thank the Mahamid Lab members for fruitful discussions, especially Mauricio Toro-Nahuelpan for help in grid preparation, Liang Xue and Edoardo D'Imprima for help in RELION data analysis. We thank Giulia Zanetti, Daniel Castano-Diez, and Beata Turonova for advice on subtomogram averaging strategies. We are grateful to Dimitry Tegunov for developing helical symmetry functionality in M. The cryo-confocal laser scanning microscope (TCS SP8-Cryo CLEM) was developed in collaboration with Leica Microsystems, and we thank Jan De Bock and Martin Schorb for invaluable input and support. We thank Jan Kosinski, Martin Beck and Petr Chlanda for critical reading of the manuscript. H.K.H.F was supported by a fellowship from the EMBL Interdisciplinary Postdoctoral Program (EI3POD) under Marie Skłodowska-Curie Actions COFUND (664726). J.M. acknowledges funding from the EMBL and a European Research Council starting grant (3DCellPhase- 760067).

Author contributions

X.Z. and J.M. conceived the project. X.Z. collected and analyzed LM, cryo-confocal, negative-staining EM data, prepared samples for PCR, western blot, mass spectrometry, transcriptome sequencing and cryo-ET, collected and processed cryo-ET data and built the model, with supervision from J.M. S.S. conducted mass spectrometry experiments and analyzed the data with supervision from M.M.S. I.Z. maintained the persistent infection cell line, preformed western blot, prepared plasmids, and assisted LM experiments. C.E.O. conducted quantitative PCR experiments and analyzed the data. C.C. and T.P. assisted in the cryo-ET data analysis of the *in situ* and isolated nucleocapsids. H.K.H.F., under the supervision of C.W.M., helped with sucrose gradient fractionation and wrote scripts for generating CLEM overlay images. I.P. provided the cell line and helped with LM. A.A.H. advised on the project, provided additional interpretations and implications. X.Z., J.M. and S.S. made figures. X.Z. and J.M. wrote the manuscript with input from all authors.

Competing interest declaration

A.A.H. is a founder and scientific advisory board member of Dewpoint Therapeutics and a founder of Caraway Therapeutics. All authors declare no competing interests.

Data availability

Structures for initial model building and analysis of interaction interfaces were obtained from the Protein Data Bank (PDB) with accession codes 4XJN (PIV5 nucleocapsid-RNA complex) and 6V85 (PIV5 L-P complex), and the Electron Microscopy Data Bank (EMDB) under accession code EMD-21095 (EM map of PIV5 L-P complex). Tomograms and the maps determined here are deposited in EMDB under accession codes EMD-13133 (majority class, isolated), EMD-13136 (minority class, isolated), EMD-13137 (straight *in situ*), EMD-13165 (viral factory at non-stressed condition), EMD-13166 (viral factory at 1 h of 0.5mM As(III) stress), and EMD-13167 (viral factory at 6 h of 30 µM As(III) stress). The associated model is deposited in the PDB under accession code 7OZR. The raw micrographs are deposited in the Electron Microscopy Public Image Archive under accession codes EMPIAR-10751 (isolated nucleocapsids). Mass spectrometry data are deposited in PRIDE. Data are available via ProteomeXchange with identifier PXD026799.

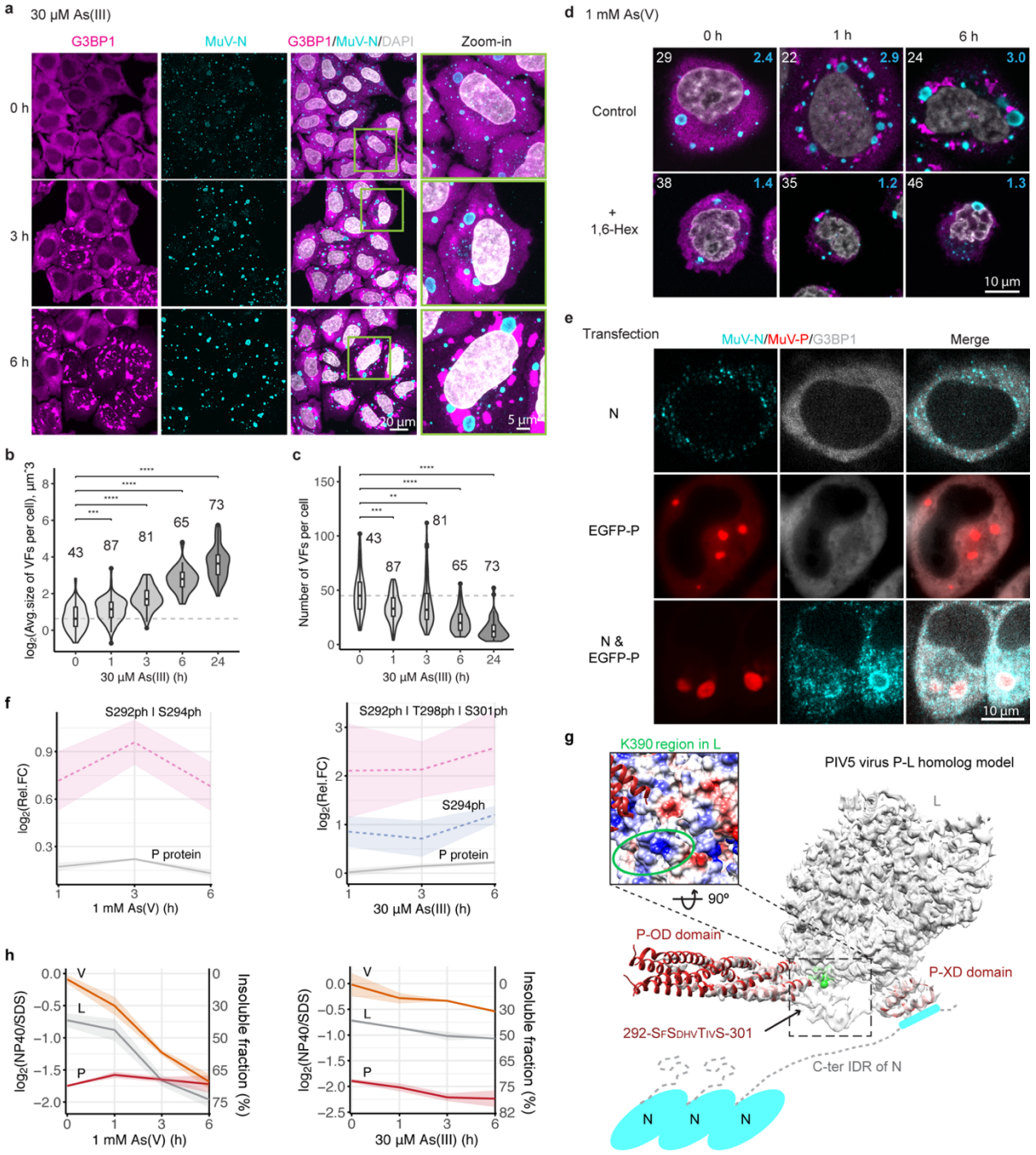

Fig. 1 | MuV factories in chronic infection are liquid-like condensates and are altered following stress. a, Confocal maximum-intensity projections of MuV factories during 30 μM As(III) treatment, detected by anti-MuV N immunostaining and mCherry-G3BP1 as a marker of stress response. Also see Extended Data Fig. 1c. **b** and **c,** Quantification of data in **a** for MuV factories size (in log2 scale) and number per cell. VFs: viral factories. The number of cells per condition is indicated. Violin plots represent relative densities. Box center line, median; box bounds, the first and third quartiles; whiskers extending from box bounds, values no further than 1.5 the distance between the first and third quartiles; data beyond the end of whiskers are shown as individual points. Dashed line indicates median at the start of stress. Statistical significance was evaluated using Wilcoxon test between later time points and the start of stress and encoded as $^{**}P<0.01$, $^{***}P<0.001$, and $^{****}P<0.0001$. **d,** MuV factories along 6 h of 1 mM As(V) stress followed by 15 min incubation with 1,6-hexanediol or water as control. Central plane images are shown. The number of cells per condition is indicated at left corners; number on the right corner is the average number of MuV factories larger than 3 μm in diameter per cell at each condition. **e,** Transfection of MuV N (detected by immunostaining) or EGFP-P plasmids into naive HeLa mCherry-G3BP1. **f,** Fold changes

(FC; in log2 scale) of P along 1 mM As(V) or 30 μM As(III) time course relative to control: unmodified protein (solid line) and phosphopeptides (dashed lines). Lines and shaded areas are mean and SEM of three biological replicates. **g,** P phosphosites mapped onto Parainfluenza virus 5 (PIV5) P-L complex structure (EMD-21095, PDB 6V85) to the unmodeled region of P (arrow). Inset: rotated view of the predicted interaction interface on L (K390 region denoted by green circle), colored according to electrostatic potential (blue to red: positively to negatively charged). P-OD: oligomerization domain of P; P-XD: C-terminal X domain of P; also see Extended Data Fig. 2e. Schematic model of N is shown to indicate the context of P-L complex, with the C-terminal IDR of N predicted to interact with the P-XD. **h,** Solubility profiles of P, V, and L proteins along 1 mM As(V) or 30 μM As(III) stress time course. Solubility is defined by NP40/SDS ratio, indicating the proportion of soluble protein in the lysate pelleting assay. Lines and shaded areas are mean and SEM of two biological replicates.

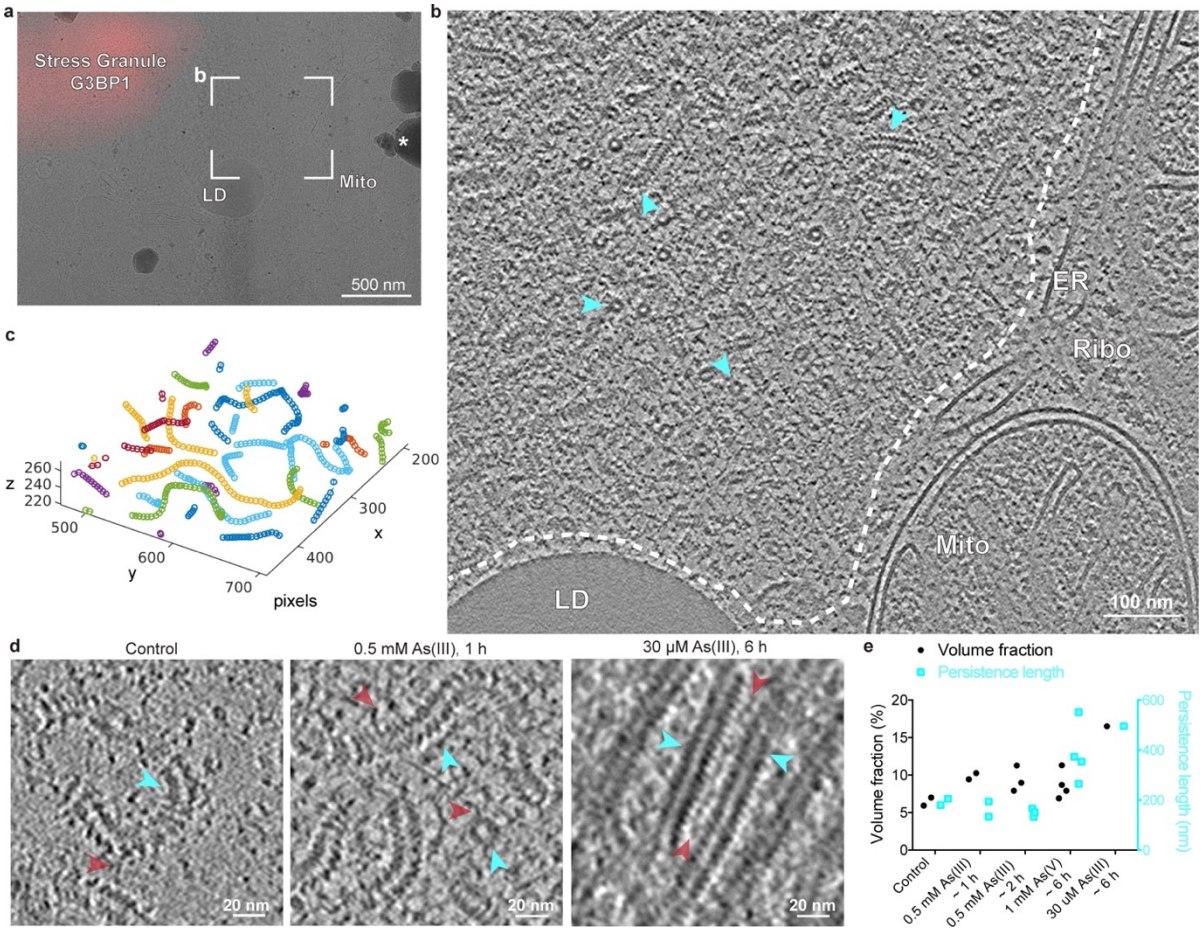

Fig. 2 | MuV nucleocapsids and viral factories undergo structural changes following stress. a, cryo-TEM image of a cryo-FIB lamella from HeLa-MuV cells after 1 h of 0.5 mM As(III) stress. Lamella was prepared by 3D targeting of mCherry-G3BP1 of stress granules (red) in proximity to a MuV factory (framed region; tomogram shown in **b**). LD: lipid droplet; Mito: mitochondria; asterisk: ice contaminant. **b,** Tomographic slice of a MuV factory. Examples of nucleocapsids are indicated with cyan arrowheads (top and side views, two of each). Neighboring organelles are labeled as in **a**. ER: endoplasmic reticulum. Ribo: ribosomes. **c,** Zoom-in view of traced nucleocapsids in **b**. Discontinuous filaments are colored separately. Traces are sampled equidistantly for subsequent quantitative analyses. **d,** Representative tomographic slices of nucleocapsids (cyan arrowheads) at indicated conditions. Slice thickness: 6.74 nm, 6.74 nm, and 6.52 nm. Red arrowheads indicate flexible densities extending from nucleocapsids. **e,** Scatter plot of volume fractions and persistence length of nucleocapsids in tomograms acquired at indicated conditions.

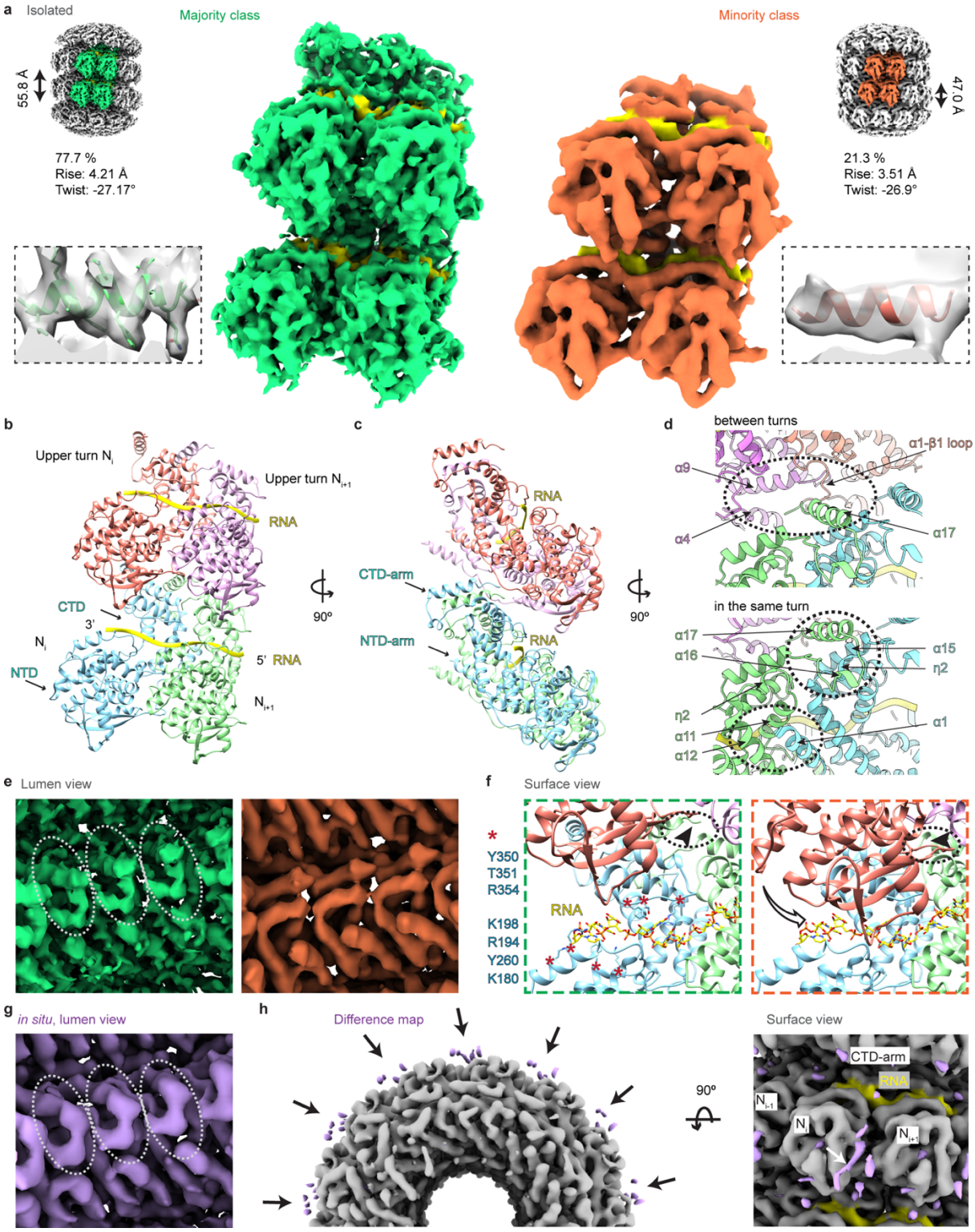

Fig. 3 | Structures of MuV nucleocapsids reveal two packing modes and variable surface accessibility of RNA and C-terminal IDRs. a, Subtomogram averages of MuV nucleocapsids extracted from HeLa-MuV cells after ~1 h of 0.5 mM As(III) stress. The two class averages exhibiting different helical parameters were resolved to 4.5 Å (left, majority class, green) and 6.3 Å (right, minority class, orange). Regions corresponding to RNA densities are colored in yellow. Four subunits are shown at scale to illustrate the packing. **b-d,** Cartoon representation of the atomic model of four MuV-N protein subunits with RNA (yellow) for the majority class. Domains of the core structure of N_i (3-405) are labeled. **d,** Packing of subunits between neighboring turns (upper) and within the same turn (lower). Circles indicate the packing interfaces. Subunits are colored as in **b-c**. **e,** Lumen

view comparison of the two classes in **a**. CTD-arms of three neighboring subunits (circled) are not resolved in the minority class (orange). **f,** Surface view comparison of the two classes. Subunits are colored as in **b-d**. RNA in stick representation and colored by heteroatom. Arrow indicates a shift of upper subunit (orange) towards the lower turn RNA binding pocket in the minority class (orange frame). Dotted circle indicates unoccupied space in the majority class (left) becomes occupied in the minority class (right), which blocks access of the C-terminus (arrowheads) to the nucleocapsid surface. Key residues potentially responsible for RNA binding are labeled (red asterisks on the left). **g,** Lumen view of the in-cell MuV nucleocapsid 6.5 Å map, generated from combined datasets of 1 mM As(V) and 30 μM As(III) stress at 6 h. CTD-arms of three neighboring subunits are encircled. **h,** Cross-section (left) and surface (right) views of the difference maps (purple) between the majority class in **a** (grey) and the in-cell nucleocapsids in **g**. Black arrows (left) and white arrow (right) indicate potential location of the C-terminal IDR at the interface between neighboring subunits. RNA regions are colored in yellow.

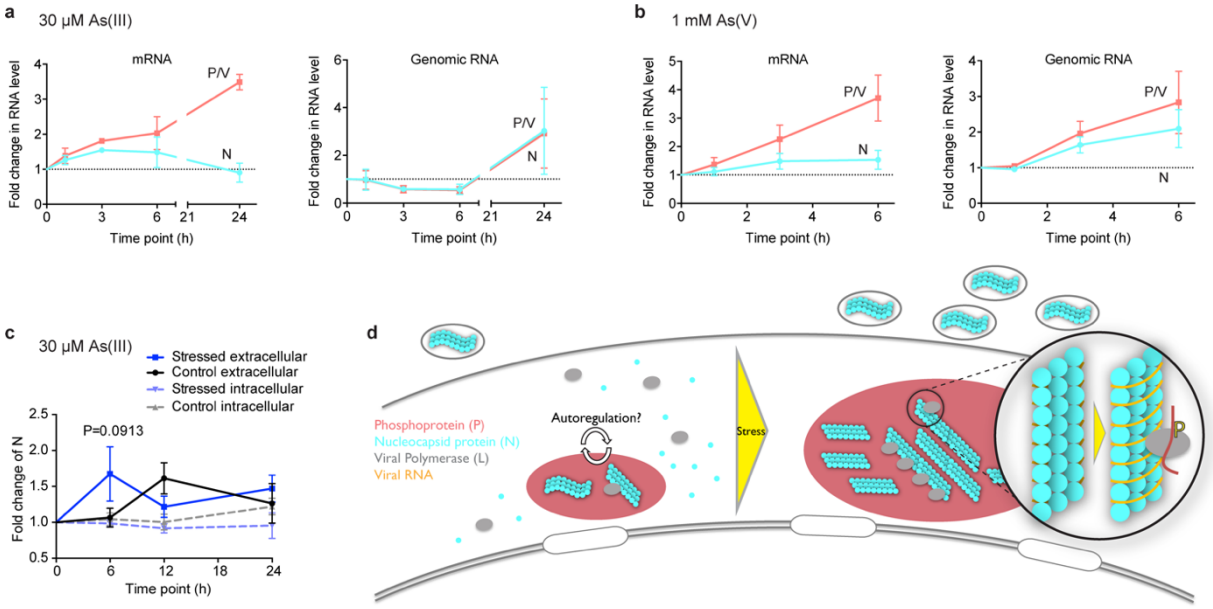

Fig. 4 | Induction of viral transcription, replication and release upon stress. a-b, quantitative PCR of MuV transcription and replication levels determined by targeting N and P/V genes during the time course of 30 μM As(III) stress (**a**) or 1 mM As(V) stress (**b**). Dotted lines indicate the starting levels. Data are the mean ± SD of three biological replicates. **c,** Quantification of ratio of MuV N protein in the cell culture medium to that inside cells detected by western blot, normalized to levels at 0 h for each condition. Data are the mean ± SEM of four independent experiments. P-value was determined by two-way ANOVA. Adjusted p-value (Bonferroni's multiple comparisons test) < 0.1 was considered significantly different. Unlabeled are not significant. **d,** Proposed model for stress-induced activation of viral replication in phase-separated MuV factories.

References

1 Hashimoto, S. *et al.* Mumps Virus Induces Protein-Kinase-R-Dependent Stress Granules, Partly Suppressing Type III Interferon Production. *PLoS One* **11**, e0161793, doi:10.1371/journal.pone.0161793 (2016).

2 Okonski, K. M. & Samuel, C. E. Stress granule formation induced by measles virus is protein kinase PKR dependent and impaired by RNA adenosine deaminase ADAR1. *J Virol* **87**, 756-766, doi:10.1128/JVI.02270-12 (2013).

3 Ruggieri, A. *et al.* Dynamic oscillation of translation and stress granule formation mark the cellular response to virus infection. *Cell Host Microbe* **12**, 71-85, doi:10.1016/j.chom.2012.05.013 (2012).

4 Bonenfant, G. *et al.* Zika Virus Subverts Stress Granules To Promote and Restrict Viral Gene Expression. *J Virol* **93**, doi:10.1128/JVI.00520-19 (2019).

5 Virgin, H. W., Wherry, E. J. & Ahmed, R. Redefining chronic viral infection. *Cell* **138**, 30-50, doi:10.1016/j.cell.2009.06.036 (2009).

6 Yokota, S. *et al.* Suppression of thermotolerance in mumps virus-infected cells is caused by lack of HSP27 induction contributed by STAT-1. *The Journal of biological chemistry* **278**, 41654-41660, doi:10.1074/jbc.M305701200 (2003).

7 Walker, D. L. & Hinze, H. C. A carrier state of mumps virus in human conjunctiva cells. I. General characteristics. *The Journal of experimental medicine* **116**, 739-750, doi:10.1084/jem.116.5.739 (1962).

8 Truant, A. L. & Hallum, J. V. A persistent infection of baby hamster kidney-21 cells with mumps virus and the role of temperature-sensitive variants. *J Med Virol* **1**, 49-67, doi:10.1002/jmv.1890010108 (1977).

9 Morfopoulou, S. *et al.* Deep sequencing reveals persistence of cell-associated mumps vaccine virus in chronic encephalitis. *Acta Neuropathol* **133**, 139-147, doi:10.1007/s00401-016-1629-y (2017).

10 Chou, S. M. Inclusion body myositis: a chronic persistent mumps myositis? *Hum Pathol* **17**, 765-777, doi:10.1016/s0046-8177(86)80197-6 (1986).

11 Guillen-Boixet, J. *et al.* RNA-Induced Conformational Switching and Clustering of G3BP Drive Stress Granule Assembly by Condensation. *Cell* **181**, 346-361 e317, doi:10.1016/j.cell.2020.03.049 (2020).

12 Cox, R. *et al.* Structural studies on the authentic mumps virus nucleocapsid showing uncoiling by the phosphoprotein. *Proceedings of the National Academy of Sciences of the United States of America* **111**, 15208-15213, doi:10.1073/pnas.1413268111 (2014).

13 Duc-Nguyen, H. & Rosenblum, E. N. Immuno-electron microscopy of the morphogenesis of mumps virus. *J Virol* **1**, 415-429, doi:10.1128/JVI.1.2.415-429.1967 (1967).

14 Berry, J., Weber, S. C., Vaidya, N., Haataja, M. & Brangwynne, C. P. RNA transcription modulates phase transition-driven nuclear body assembly. *Proceedings of the National Academy of Sciences of the United States of America* **112**, E5237-5245, doi:10.1073/pnas.1509317112 (2015).

15 Zwicker, D., Hyman, A. A. & Julicher, F. Suppression of Ostwald ripening in active emulsions. *Phys Rev E Stat Nonlin Soft Matter Phys* **92**, 012317, doi:10.1103/PhysRevE.92.012317 (2015).

16 Zhou, Y., Su, J. M., Samuel, C. E. & Ma, D. Measles Virus Forms Inclusion Bodies with Properties of Liquid Organelles. *J Virol* **93**, doi:10.1128/JVI.00948-19 (2019).

17 Guseva, S. *et al.* Measles virus nucleo- and phosphoproteins form liquid-like phase-separated compartments that promote nucleocapsid assembly. *Sci Adv* **6**, eaaz7095, doi:10.1126/sciadv.aaz7095 (2020).

18 Risso-Ballester, J. *et al.* A condensate-hardening drug blocks RSV replication in vivo. *Nature*, doi:10.1038/s41586-021-03703-z (2021).

19 Iserman, C. *et al.* Genomic RNA Elements Drive Phase Separation of the SARS-CoV-2 Nucleocapsid. *Mol Cell* **80**, 1078-1091 e1076, doi:10.1016/j.molcel.2020.11.041 (2020).

20 Lu, S. *et al.* The SARS-CoV-2 nucleocapsid phosphoprotein forms mutually exclusive condensates with RNA and the membrane-associated M protein. *Nat Commun* **12**, 502, doi:10.1038/s41467-020-20768-y (2021).

21 Wheeler, J. R., Matheny, T., Jain, S., Abrisch, R. & Parker, R. Distinct stages in stress granule assembly and disassembly. *Elife* **5**, doi:10.7554/eLife.18413 (2016).

22 Wang, J. *et al.* A Molecular Grammar Governing the Driving Forces for Phase Separation of Prion-like RNA Binding Proteins. *Cell* **174**, 688-699 e616, doi:10.1016/j.cell.2018.06.006 (2018).

23 Cox, R. *et al.* Characterization of a mumps virus nucleocapsidlike particle. *J Virol* **83**, 11402-11406, doi:10.1128/JVI.00504-09 (2009).

24 Pickar, A. *et al.* Oligomerization of Mumps Virus Phosphoprotein. *J Virol* **89**, 11002-11010, doi:10.1128/JVI.01719-15 (2015).

25 Sridharan, S. *et al.* Proteome-wide solubility and thermal stability profiling reveals distinct regulatory roles for ATP. *Nat Commun* **10**, 1155, doi:10.1038/s41467-019-09107-y (2019).

26 Abdella, R., Aggarwal, M., Okura, T., Lamb, R. A. & He, Y. Structure of a paramyxovirus polymerase complex reveals a unique methyltransferase-CTD conformation. *Proceedings of the National Academy of Sciences of the United States of America* **117**, 4931-4941, doi:10.1073/pnas.1919837117 (2020).

27 Yokosawa, N., Yokota, S., Kubota, T. & Fujii, N. C-terminal region of STAT-1alpha is not necessary for its ubiquitination and degradation caused by mumps virus V protein. *J Virol* **76**, 12683-12690, doi:10.1128/jvi.76.24.12683-12690.2002 (2002).

28 Kubota, T., Yokosawa, N., Yokota, S. & Fujii, N. Association of mumps virus V protein with RACK1 results in dissociation of STAT-1 from the alpha interferon receptor complex. *J Virol* **76**, 12676-12682, doi:10.1128/jvi.76.24.12676-12682.2002 (2002).

29 Rosas-Murrieta, N. H., Herrera-Camacho, I., Palma-Ocampo, H., Santos-Lopez, G. & Reyes-Leyva, J. Interaction of mumps virus V protein variants with STAT1-STAT2 heterodimer: experimental and theoretical studies. *Virol J* **7**, 263, doi:10.1186/1743-422X-7-263 (2010).

30 Angers, S. *et al.* Molecular architecture and assembly of the DDB1-CUL4A ubiquitin ligase machinery. *Nature* **443**, 590-593, doi:10.1038/nature05175 (2006).

31 Becher, I. *et al.* Pervasive Protein Thermal Stability Variation during the Cell Cycle. *Cell* **173**, 1495-1507 e1418, doi:10.1016/j.cell.2018.03.053 (2018).

32 Liljeroos, L., Huiskonen, J. T., Ora, A., Susi, P. & Butcher, S. J. Electron cryotomography of measles virus reveals how matrix protein coats the ribonucleocapsid within intact virions. *Proceedings of the National Academy of Sciences of the United States of America* **108**, 18085-18090, doi:10.1073/pnas.1105770108 (2011).

33 Katoh, H. *et al.* Heat shock protein 70 regulates degradation of the mumps virus phosphoprotein via the ubiquitin-proteasome pathway. *J Virol* **89**, 3188-3199, doi:10.1128/JVI.03343-14 (2015).

34 Cox, R. *et al.* Structural and functional characterization of the mumps virus phosphoprotein. *J Virol* **87**, 7558-7568, doi:10.1128/JVI.00653-13 (2013).

35 Severin, C. *et al.* Releasing the Genomic RNA Sequestered in the Mumps Virus Nucleocapsid. *J Virol* **90**, 10113-10119, doi:10.1128/JVI.01422-16 (2016).

36 Ke, Z. *et al.* Promotion of virus assembly and organization by the measles virus matrix protein. *Nat Commun* **9**, 1736, doi:10.1038/s41467-018-04058-2 (2018).

37 Shan, H. *et al.* Structural plasticity of mumps virus nucleocapsids with cryo-EM structures. *Commun Biol* **4**, 833, doi:10.1038/s42003-021-02362-0 (2021).

38 Cox, R. M., Krumm, S. A., Thakkar, V. D., Sohn, M. & Plemper, R. K. The structurally disordered paramyxovirus nucleocapsid protein tail domain is a regulator of the mRNA transcription gradient. *Sci Adv* **3**, e1602350, doi:10.1126/sciadv.1602350 (2017).

39 Thakkar, V. D. *et al.* The Unstructured Paramyxovirus Nucleocapsid Protein Tail Domain Modulates Viral Pathogenesis through Regulation of Transcriptase Activity. *J Virol* **92**, doi:10.1128/JVI.02064-17 (2018).

40 Bhella, D., Ralph, A. & Yeo, R. P. Conformational flexibility in recombinant measles virus nucleocapsids visualised by cryo-negative stain electron microscopy and real-space helical reconstruction. *J Mol Biol* **340**, 319-331, doi:10.1016/j.jmb.2004.05.015 (2004).

41 Jensen, M. R. *et al.* Intrinsic disorder in measles virus nucleocapsids. *Proceedings of the National Academy of Sciences of the United States of America* **108**, 9839-9844, doi:10.1073/pnas.1103270108 (2011).

42 Doi, T. *et al.* Measles virus induces persistent infection by autoregulation of viral replication. *Sci Rep* **6**, 37163, doi:10.1038/srep37163 (2016).

Methods

Cells and virus

HeLa cell line stably expressing mCherry-G3BP1 by bacterial artificial chromosome tagging[43] was previously described[11]. Cells were cultured in Dulbecco's modified Eagle's medium (DMEM, high glucose, GlutaMAX Supplement, Gibco) supplemented with 10% fetal bovine serum, 50 U/ml Penicilin-Streptomycin and 2 µg/ml Blasticidin S (Gibco), and maintained using standard procedures. The MuV persistently infected cell line (HeLa-MuV) was generated by infecting the HeLa mCherry-G3BP1 cells with MuV strain Enders (single nucleotide variations in Supplementary Data 1) and re-establishment of cell growth was observed after ~20 days[44].

Stress treatment and confocal light microscopy

For fluorescent microscopy, HeLa-MuV cells (mCherry-G3BP1) were seeded on 35-mm dishes with glass bottom the day before stress treatment. Cells were stressed by replacing the culture medium with that containing either 0.5 mM sodium arsenite (referred to as As(III)) for up to 3 h, 1 mM potassium arsenate (referred to as As(V)) for up to 6 h, 30 µM As(III) for up to 24 h, or transferring the cell culture dishes to an incubator set to 43 °C for 1 h of heat shock. Samples of all time points in particular stress condition were fixed at once with 4% paraformaldehyde (PFA) pH 7.4 in phosphate-buffered saline (PBS; 2.67 mM KCl, 1.5 mM KH_2PO_4, 137 mM NaCl, and 8.1 mM NaH_2PO_4, pH 7.4) for 10 min, after rinsing twice with PBS. Samples were rinsed with cold PBS and permeabilized with 0.2% Trion X-100 for another 10 min. Samples were blocked with 1% bovine serum albumin (BSA) for 30 min, incubated with mouse monoclonal antibody against MuV N protein (1:200; clone 8H4; Abcam, ab9876) diluted in 1% BSA for 1 h at room temperature and then with goat anti-mouse IgG secondary antibody Alexa Fluor 488 (1:2,000; highly cross-adsorbed; Invitrogen, A-11029). The samples were finally immersed in ProLong Gold Antifade Mountant formulated with the DNA stain DAPI (Thermo Fisher Scientific) and sealed. Confocal imaging was performed on a Zeiss LSM780 inverted microscope with a 63× 1.40 NA oil immersion objective and a GaAsP spectral detector. Settings were kept the same for imaging samples of all time points in one experiment. Z-stack images were segmented using the Imaris software (Oxford Instruments) using the Surface module. Surfaces of viral factories were generated by absolute intensity thresholding with a fixed value for the anti-N staining signal in each dataset (values optimized for different datasets) and surfaces of nuclei by background subtraction auto-thresholding of the DAPI staining signal, separately. Distances between viral factories and nuclei were calculated for each image stack with MATLAB (MathWorks) scripts to assign viral factories to individual cells. Volumes and numbers of viral factories per cell were then used for generating density plots with RStudio scripts.

All light microscopy figures were prepared with FIJI[45]. Maximum intensity projected images are shown for Z-stack images.

Hexanediol treatment

Hexanediol treatment was done for assessing the liquid-like properties of viral factories at 1 mM As(V) stress conditions. Culture medium was replaced with medium containing 1 mM As(V) as before for 1 h or 6 h to induce stress. Together with the unstressed cell samples as 0 h control, cells were either immediately fixed as control for each time point, or incubated with 3.5% 1,6-hexanediol (Sigma-Aldrich) or water for 15 to 30 min and then fixed. Immunostaining and imaging were done as described above. Central slice images were acquired. 2D segmentation was similarly done using the surface module in Imaris software. The number of viral factories larger than 7.07 μm^2 (diameter over 3 µm assuming a sphere) per cell was counted for each condition.

Transfection

Transfection was done with the untagged N and mEGFP (monomeric enhanced green fluorescent protein) tagged P plasmids into naïve HeLa mCherry-G3BP1 cells (not infected by MuV). The genes were synthesized by GeneArt Gene Synthesis (Thermo Fisher Scientific) both in a pcDNA3.1 vector and the mEGFP gene was then inserted at the N-terminus of P gene. Transfection was done on pre-seeded HeLa cells (70% confluency) with the FuGENE 6 Transfection Reagent (Promega) following standard protocol. At 48 h after transfection, cells were fixed and immunostained as described above. Imaging was performed on a PerkinElmer spinning disk confocal microscope with a 63× 1.40 NA oil immersion objective and a Hamamatsu EMCCD camera. Central slice images were acquired.

Quantitative PCR

0.5 to 1 million cells per condition and time point were used for isolating total RNA. The extraction was performed according to manufacturer's instructions using the RNeasy Micro Kit (Qiagen). Strand-specific reverse transcription of genomic RNA (gRNA), anti-genomic RNA (cRNA) and mRNA was performed with the 3'-UTR genomic forward primer, L-gene antigenomic reverse primer (Supplementary Table), and oligo $d(T)_{23}$ primer (New England Biolabs) for transcripts. For quantitative comparison between samples, cDNA was also generated for the cellular control gene RNase P using a gene specific reverse primer (Supplementary Table). 1 µg of RNA was used to generate specific cDNAs for each condition, time point and target gene separately. Synthesis was performed according to manufacturer's instructions using the ProtoScript II Reverse Transcriptase Kit (NEB).

Real-time quantitative PCR (qPCR) assay was performed using TaqPath qPCR Master Mix, CG (Thermo Fisher Scientific), target-specific primers and Taqman probes (Supplementary Table). 20× primer probe mixes of each target gene were prepared with 150 nM forward primers, 150 nM reverse primers and 100 nM taqman probes. Genome, and antigenomic cDNAs were mixed with the cellular control gene RNase P cDNA for each condition and time point at a dilution of 1:10. Transcript cDNAs

generated with the oligo $d(T)_{23}$ primer were diluted at 1:10 for each condition and time point. The qPCR was set up in 10 µl total mixture comprised of 5 µl Master Mix (2×), 0.5 µl N-gene primer-probe mix, 0.5 µl P-gene primer-probe mix, 0.5 µl F-gene primer-probe mix, 0.5 µl RNaseP control gene primer-probe mix, 2 µl H_2O, and 1 µl cDNA mixes (1:10 dilution). Within each plate, standard curves were included at the dilution range of 1:10 to 1:10,000 with the non-treated control condition of each biological replica. qPCR was performed using the Roche LightCycler96 cycling conditions: 95 ºC for 20 sec for polymerase activation followed by 45 cycles of 95 ºC for 15 sec denaturation and 60 ºC for 60 sec annealing and extension. The Taqman probes were detected with the filter sets 470/514 nm for FAM, 533/572 nm for HEX, 577/620 nm for LC610, and 645/697 nm for Cy5.

Fold changes were calculated relative to the non-treated 0 h time point of each condition and biological replica. Data was normalized against RNase P internal control. qPCR efficiency values were calculated for each biological replica and included for fold change calculations. The average was calculated for three independent biological replicas to obtain the fold change of genomic and anti-genomic viral load, and transcriptional mRNA levels for each target gene. Data were analyzed with GraphPad Prism 6.0c.

Transcriptome sequencing

HeLa-MuV cells after ~1 h of 0.5 mM As(III) were used for isolating total RNA according to manufacturer's instructions using the RNeasy Micro Kit (Qiagen). Briefly, RNA integrity was checked using the RNA Nano 6000 Assay Kit of the Bioanalyzer 2100 system (Agilent Technologies), and concentration was measured with Qubit RNA Assay Kit in Qubit 2.0 Fluorometer (Life Technologies). Stranded mRNA-Seq libraries were prepared from 250 ng of total RNA using the NEBNext Ultra II Directional RNA Library Prep Kit for Illumina (New England Biolabs) implemented on the liquid handling robot Beckman i7. The protocol starts with the isolation of mRNA from total RNA by a polyA selection with oligo d(T) beads, followed by fragmentation and priming of mRNA with random primers to generate double-stranded cDNA fragments. Subsequently, adaptors were ligated to cDNA fragments, which were then amplified with 13 PCR cycles and purified with SPRIselect beads (Beckman Coulter). Fragmentation time purification steps were optimized to allow the selection of larger fragment sizes (>200 nt). Size distribution of the final library was assessed on Bioanalyzer with a DNA High Sensitivity kit (Agilent Technologies), and concentration was measured with Qubit DNA High Sensitivity kit in Qubit 2.0 Fluorometer. Final libraries were pooled in equimolar amounts and loaded at 2 pM solution on the Illumina sequencer NextSeq 500 MID output and sequenced uni-directionally, generating ~150 million reads per run, each 155 bases long.

Sequencing reads were aligned using BWA-MEM (v0.7.17-r1188) with default parameters to the Enders strain of Mumps virus (GU980052). Duplicated reads were then filtered out using MarkDuplicates function in Picard tool (v2.9.0-1-gf5b9f50-SNAPSHOT). FreeBayes (v1.1.0-3-

g961e5f3) was used to call single nucleotide variations compared to the Enders strain sequence. Finally, the variants were filtered based on their qualities (> 20).

Western blot

HeLa-MuV cells were seeded ~24 h prior to the start of stress treatment in T-25 flasks for each sample. Stress treatment was performed by adding 100 uL of 1.5 mM sodium arsenite solution into each T-25 flask (final concentration of 30 µM in 5 mL culture medium each) and gently mixing it with culture medium. Samples were collected at four time points- 0 h, 6 h, 12 h, 24 h, for both stressed and control samples. First, the culture medium of each was separately collected for subsequent enrichment of the released N protein. Then, cell pellet samples were collected via direct lysis by adding 1% SDS dissolved in PBS, with 1.5 mM $MgCl_2$, EDTA-free protease inhibitor cocktail (cOmplete, Roche) and 1 mM PMSF. 0.3 µl of Benzonase (250 U/µl, Millipore) was added to each flask and the flasks were shaken on a shaking platform (Eppendorf Thermomixer Compact) at 750 RPM for 15-20 min until the jelly substance disappeared. The cell lysate was then recovered from the flasks, adjusted to the same volume, heated at 95 ºC for 5 min and frozen for further use. Processing of the culture medium containing the released viral proteins was started by centrifugation at 2,200 *g*, 4 ºC for 15 min to remove cell debris. Then, the supernatant was mixed with 4× concentration solution (40% PEG 6,000, 100 mM HEPES, pH 7.5, and 2 M NaCl, with EDTA-free protease inhibitor cocktail and 1 mM PMSF) thoroughly and left at 4 ºC. After ~24 h of precipitation, the samples were centrifuged at 4,300 *g*, 4 ºC for 30 min. After careful removal of the supernatant, a white disk was seen at each tube bottom, and recovered with the same lysis buffer as for cell pellets. Volumes of these samples containing the released viral proteins were also adjusted to the same for all samples, heated at 95 ºC for 5 min and frozen for further use.

Total protein concentration of each cell lysate sample was determined by Bradford assay with Protein Assay Dye (Bio-Rad) on a UV/Visible spectrophotometer (Ultrospec 2100 pro, Amersham Biosciences). For western blot analysis, volume corresponding to ~20 µg total protein was taken for each cell lysate sample and supplemented to the same volume for all samples before the loading buffer with reducing agent was added. The samples containing the released viral proteins were also volume adjusted according to the total protein concentration in their respective cell lysate sample so that the comparison will be performed with the same total intracellular protein level among all time points, for both the stressed and control samples. Proteins were separated using NuPAGE 4-12% precast Bis-Tris protein gels in MOPS SDS running buffer (Invitrogen), transferred onto Immobilon-P PVDF membranes (Millipore), and analyzed with mouse monoclonal antibodies against MuV-N (1:1,000; clone 8H4; Abcam, ab9876) and glyceraldehyde-3-phosphate dehydrogenase (GAPDH, 1:4,000; clone 6C5; Santa Cruz, sc-32233) as loading control. Goat anti-mouse IgG (H/L):HRP (1:1,000; multi species absorbed; Bio-Rad, STAR117P) and ECL western blot detection reagents (Cytiva) were then used for detection with a ChemiDoc Imager (Bio-Rad). Intensity quantification was done in Image Lab (v6.1;

Bio-Rad). To calculate the intracellular levels of MuV-N over time (fold change), the intensity of N in cell lysate samples was normalized to the intensity of the respective loading control (GAPDH) and shown as relative to 0 h. To analyze the released levels of N over time (fold change), the intensity of MuV-N in samples containing the released viral proteins was divided by the intensity of MuV-N in the respective cell lysate sample and shown as relative to 0 h. Data were analyzed with GraphPad Prism 6.0c.

Mass spectrometry (MS) cell lysate preparation

Whole cell lysate preparation

Cells were stressed as described above. At the indicated time points, cells were detached by trypsinization, washed and pelleted twice with PBS. For total proteome analysis, 0.5 million cells per condition were lysed with 100 µl of PBS containing 1.5 mM $MgCl_2$, 1% SDS and 0.25 U/µl Benzonase and incubated at room temperature for 15 min. The protein concentration in cell lysates were determined using a BCA assay. Cell lysate volumes corresponding to 5 µg total protein from different conditions were utilized for MS sample preparation.

Solubility proteome profiling (SPP) lysate preparation

One cell pellet containing 1 million cells was frozen per time point following cellular stress (as described above). The cell pellets were thawed on ice and lysed (3 freeze thaw cycles) after re-suspending each one in 100 µl of PBS containing protease inhibitors (Roche), 0.8 % NP40, 1.5 mM $MgCl_2$ and phosphatase inhibitor (Roche). The lysate was split into two 50 µl aliquots. One aliquot was spun at 100,000g, 20 min at 4˚C and the supernatant was retrieved. This represented the "soluble-NP40" fraction of proteins. The second aliquot was further solubilized with SDS (final concentration 1%). This represented the "total-SDS" proteome. Both aliquots were incubated with Benzonase (final concentration 0.25 U/µl). The protein concentration of total proteome fractions was determined with BCA assay. Volumes of total lysate corresponding to 5 µg protein from different conditions were calculated. Equal volume of the soluble-NP40 samples to its corresponding total lysate was utilized. Both soluble and total lysate of each condition over the time course was multiplexed as a single MS experiment.

MS sample preparation

MS sample preparation and measurements were performed as described[25,46]. Protein digestion was performed using a modified SP3 protocol[46,47]. 5 µg of proteins (per condition) were diluted to a final volume of 20 µl with 0.5% SDS and mixed with a paramagnetic bead slurry (10 µg beads (Sera-Mag Speed beads, Thermo Fischer Scientific) in 40 µl ethanol). The mixture was incubated at room temperature with shaking for 15 min. The beads now bound to the proteins were washed 4 times with 70% ethanol. Proteins on beads were reduced, alkylated and digested using 0.2 µg trypsin, 0.2µg LysC,

1.7 mM TCEP and 5 mM chloroacetamide in 100 mM HEPES, pH 8. Following an overnight incubation, the peptides were eluted from the beads, dried under vacuum, reconstituted in 10 µl of water and labelled with TMT-10 or TMT-16plex reagents and dissolved in acetonitrile at 1:15 (peptide:TMT weight ratio) for one hour at room temperature. The labelling reaction was quenched with 4 µl of 5% hydroxylamine and the conditions belonging to a single MS experiment were pooled together. The pooled sample was desalted with solid-phase extraction after acidification with 0.1 % formic acid. The samples were loaded on a Waters OASIS HLB µelution plate (30 µm), washed twice with 0.05% formic acid and finally eluted in 100 µl of 80% acetonitrile containing 0.05% formic acid. The desalted peptides were dried under vacuum and reconstituted in 20 mM ammonium formate. The samples were fractionated using C18-based reversed-phase chromatography running at high pH. Mobile phases constituted of 20 mM Ammonium formate pH 10 (buffer A) and acetonitrile (buffer B). This system was run at 0.1 ml/min on the following gradient: 0% B for 0 – 2 min, linear increase 0 - 35% B in 2 – 60 min, 35 – 85% B in 60 – 62 min, maintain at 85% B until 68 min, linear decrease to 0% in 68 – 70 min and finally equilibrated the system at 0% B until 85 min. Fractions (0.2 ml) were collected between 2 – 70 min and every 12th fraction was pooled together and vacuum dried.

LC-MS-MS measurement

Samples were re-suspended in 0.05% formic acid and analyzed on Q Exactive Plus or Orbitrap Fusion Lumos mass spectrometers (Thermo Fischer Scientific) connected to UltiMate 3000 RSLC nano system (Thermo Fisher Scientific) equipped with a trapping cartridge (Precolumn; C18 PepMap 100, 5 µm, 300 µm i.d. × 5 mm, 100 Å) and an analytical column (Waters nanoEase HSS C18 T3, 75 µm × 25 cm, 1.8 µm, 100 Å) for chromatographic separation. Mobile phase constituted of 0.1% formic acid in LC-MS grade water (Buffer A) and 0.1% formic acid in LC-MS grade acetonitrile (Buffer B). The peptides were loaded on the trap column (30 µl/min of 0.05% trifluoroacetic acid in LC-MS grade water for 3 min) and eluted using a gradient from 2% to 30% Buffer B over 2 h at 0.3 µl/min (followed by an increase to 40% B, and a final wash to 80% B for 2 min before re-equilibration to initial conditions). The outlet of the LC- system was directly fed for MS analysis using a Nanospray-Flex ion source and a Pico-Tip Emitter 360 µm OD × 20 µm ID; 10 µm tip (New Objective). The mass spectrometer was operated in positive ion mode. The spray voltage and capillary temperature was set to 2.3 kV and 275°C respectively. Full-scan MS spectra with a mass range of 375–1,200 m/z were acquired in profile mode using a resolution of 70,000 (maximum fill time of 250 msec or a maximum of 3e^6 ions (automatic gain control, AGC)). Fragmentation was triggered for the top 10 peaks with charge 2–4 on the MS scan (data-dependent acquisition) with a 30-sec dynamic exclusion window (normalized collision energy was 30), and MS/MS spectra were acquired in profile mode with a resolution of 35,000 (maximum fill time of 120 msec or an AGC target of 2e^5 ions).

MS protein identification and quantification

The MS data was processed as previously described[25]. Briefly, the raw MS data was processed with isobarQuant (and identification of peptides and proteins was performed with Mascot 2.4 (Matrix Science) against a database containing *Homo sapien* Uniprot FASTA (proteome ID: UP000005640, downloaded on 14 May 2016) and in-house sequenced and assembled encoding sequences of Mumps Enders strain (single nucleotide variations in Supplementary Data 1) along with known contaminants and the reverse protein sequences (search parameters: trypsin; missed cleavages 3; peptide tolerance 10 ppm; MS/MS tolerance 0.02 Da; fixed modifications included carbamidomethyl on cysteines and TMT10 or TMT16 plex on lysine; variable modifications included acetylation of protein N-terminus, methionine oxidation and TMT10 or 16plex on peptide N-termini). The whole cell proteome datasets were also searched with phosphorylation on S|T|Y as a variable modification.

MS Data analysis

All MS data analysis was performed using R (v.3.6.1).

Whole cell proteome data analysis

The distributions of signal sum intensities from all TMT channels was normalized with vsn[48] to correct for slight differences in protein amounts. Differential analysis was performed on log2 transformed signal sums of different stress time points and control condition using limma[49]. Proteins with $|\log_2(\text{fold change})| > 0.5$ and adjusted p-value (Benjamini Hochberg) < 0.01 were considered significantly changed.

Solubility proteome profiling data analysis

Data normalization for solubility proteome profiling experiments were performed based on a subset of proteins that are predominantly soluble. The NP40/SDS ratio of proteins was calculated using raw signal sum intensities. Proteins with NP40/SDS ratio between 0.8 and 1.2 represented the soluble subset. This subset was utilized for calculating the calibration and transformation parameters for vsn[48]. These parameters were then applied to all proteins identified to correct for technical variations. The NP40/SDS ratio was calculated using normalized signal sum intensities and log2 transformed for performing differential analysis using limma[49]. Proteins with $|\log_2(\text{fold change})| > 0.5$ and adjusted p-value (Benjamini-Hochberg) < 0.1 were considered significantly changed.

Gene ontology over representation analysis

Differentially expressed human proteins from 30 µM arsenite treatment dataset were used for GO term "Biological processes" overrepresentation analysis using clusterProfiler (R Bioconductor)[50]. All identified proteins in this dataset were used as the background. Standard settings were used for

representing enriched GO terms (p-value cutoff: 0.05, Benjamini-Hochberg procedure for multiple testing adjustment and q-value cutoff of 0.2).

Nucleocapsids isolation and negative staining electron microscopy

HeLa-MuV cells were seeded on 20-cm dishes one day prior to stress treatment. After replacing the culture medium with that containing 0.5 mM As(III) and incubating the cells for ~1 h, cells were scraped off dishes with 2 ml medium per dish, pelleted at 850 *g* for 3 min and frozen and stored at -80 ºC. On the day of experiment, the cell pellets were thawed on ice and resuspend with 250 µl of lysis buffer (50 mM Tris, pH 7.5, 100 mM KAc, 2 mM $Mg(Ac)_2$, 0.5 mM DTT, 0.5% IGEPAL CA-630, EDTA-free protease inhibitor cocktail, 1 U/µl Ribonuclease inhibitor Sigma) per vial of pellet. The following operations were done on ice unless specified. Cells were lysed with a syringe with a 27G ¾ needle for 5 passages. The lysate was centrifuged at 500 *g*, 4 °C, for 5 min to pellet cell debris. Next, the supernatant was centrifuged at 13,000 *g*, 4 °C, for 20 min. The pellet was sufficient for enriching nucleocapsids without much significant cellular contaminants. Pellets (resuspended with the lysis buffer without IGEPAL CA-630) and supernatants of each centrifugation step was used for negative staining electron microscopy (EM) experiments. Nucleocapsids in the13,000 *g* pellet resuspension were additionally supplied with heparin solution at 50 µg/ml for 2 h.

Negative staining was done with 1% uranyl acetate solution. For each sample, 2.5 µl of sample solution (1:4 to 1:100 diluted depending on concentration) was deposited on an EM copper grid (400-mesh, Plano G2400C, coated with 6 nm thick carbon produced with a Leica EM ACE600 sputter coater), incubated for 30-60 sec and manually blotted with filter paper. 2.5 µl of uranyl solution was then immediately applied to the grid and blotted away, and this step was repeated for three times. Grids were left to dry and then imaged with a Tecnai T12 EM operated at 120 kV (Thermo Fisher Scientific) at 13,000× magnification for screening and 49,000× magnification for image acquisition.

Sucrose gradient fractionation protocol was optimized in two experiments. In the initial experiment, the cell lysate after removal of cell debris at 850 *g* was first pelleted with an Optima MAX-XP Ultracentrifuge (with TLA-100 rotor, Beckman Coulter) at 35,000 rpm (47,265 *g*) 4 °C, for 40 min in order to collect most nucleocapsids. The pellet was then resuspended in lysis buffer without IGEPAL CA-630, and loaded on a 5 mL 10-65% (w/v) sucrose gradient prepared with a BioComp Gradient Master instrument. Ultracentrifugation was carried out at 35,000 rpm (116,140 *g*), 4 °C for 2 h in an Optima L-100XP ultracentrifuge (with SW 55 Ti rotor, Beckman Coulter). Fractionation was done manually by collecting every 200 µl volume from the top till the bottom of each centrifuge tube. Every other fraction was imaged by negative stain EM. Based on the images, the pellet at 35,000 rpm contains too much cellular material. Thus, the experiment was optimized for the second time, using the 13000 *g* pellet as the starting material for a sucrose gradient of 20-70%. Sucrose in fractions were removed by

dialysis with the same lysis buffer without IGEPAL CA-630, in order to reduce background for negative staining EM. Fractions around the one showing the most abundant nucleocapsids in negative staining EM were subjected to mass spectrometry analysis as described above.

Plunge freezing

The isolated nucleocapsids were prepared from the lysate of HeLa-MuV cells after 1 h of 0.5 mM As(III) stress as above (13,000 *g* pellet, 50 µg/ml heparin treated). Plunge freezing was done with a Vitrobot Mark IV (Thermo Fisher Scientific) set to 22 °C, 100 % humidity. Glow-discharged holey Quantifoil grids with an additional layer of continuous carbon (R2/1 + 2 nm C, Cu 200 mesh grid, Quantifoil Micro Tools) were used. 3 µl of nucleocapsids suspension was mixed with 1.5 µl of 10-nm colloidal gold (in the same buffer as nucleocapsids) and deposited onto grids. Grids were blotted from both sides with blot force 0 for 2 sec and drained for 2 sec before being plunged into liquid ethane at liquid nitrogen temperature. The frozen grids were stored in sealed boxes in liquid nitrogen until imaging.

Sample preparation and vitrification for cellular cryo-ET

For plunge freezing of HeLa-MuV cells under different stress conditions as described above, either a Vitrobot Mark 4 or Leica EM GP (Leica Microsystems) were used. Gold Quantifoil grids (R1/4, Au 200 mesh grid, SiO2, Quantifoil Micro Tools) were glow-discharged and UV irradiated for 30 min for sterilization before being immersed in cell culture medium in 35-mm IBIDI µ-Dish. Next, HeLa-MuV cells were seeded in such dishes each containing 5-6 grids and cultured in an incubator overnight at 37 °C and 5% CO_2. Cells cultivated on grids were plunge-frozen in liquid ethane/propane mixture at close to liquid nitrogen. The blotting conditions for the Vitrobot were set to 37 °C, 90% humidity, blot force 10, 10 sec blot time and 2 sec drain time and grids were blotted from the reverse side with the aid of a Teflon sheet from the front side. The blotting conditions for the Leica EM GP were set to 37 °C, 90% humidity, blot volume 3 µl, 2-3 s blot time and grids were also blotted from the reverse side. For grids that were used in subsequent correlative imaging, 2 µl of 1-µm crimson beads (FluoSpheres carboxylate-modified microspheres, 625/645, Thermo Fisher Scientific) diluted 1:40 from original stock were added to the grid surface from one side before blotting. Grids were stored in liquid nitrogen until usage.

Cryo-fluorescence light microscopy

Frozen grids were fixed into custom-made AutoGrid specimen cartridges modified for FIB preparation under shallow angles[51] and imaged by a prototype Leica cryo-fluorescence light microscope (FLM) based on Leica TCS SP8 CFS equipped with a cryo-stage operated at liquid nitrogen temperature[52]. The microscope includes a widefield light path and a confocal path with independent light sources and is

equipped with a 50x/0.9 NA cryo-objective. The grid overview was first acquired using widefield to find focal planes. Intact grid squares with signal of interest were then imaged with the confocal path by exciting with a 552-nm laser and simultaneously detecting at 569-633 nm and 695-700 nm with two HyD detectors. After imaging, grids were stored in liquid nitrogen for the next step.

Cryo-focused ion beam milling

Plunge-frozen grids fixed into custom-made AutoGrids were mounted into a shuttle and transferred into an Aquilos cryo-focused ion beam/scanning electron microscope (FIB/SEM dual-beam microscope, Thermo Scientific). During FIB operation, samples were kept at constant liquid nitrogen temperature. To improve sample conductivity and reduce curtaining artifacts during FIB milling, the samples were first sputter-coated with platinum and then coated with organometallic platinum using the gas injection system[53]. Lamellae were prepared using Gallium ion beam at 30 kV and stage tilt angles of 15°-20°. The MAPS software installed on the Aquilos microscope was used to refine eucentricity and record coordinates to prepare lamellae. Lamella preparation was conducted in a stepwise manner: rough milling with currents of 1 nA, gradually reduced to lower currents, down to 50 pA for the final polishing step[54]. Progress of the milling process was monitored using the SEM operated at 10 kV and 50 pA. For improving conductivity of the final lamella, we sputter-coated the grid again after cryo-FIB preparation with platinum. The thickness of the platinum layer and entire lamellae was determined from the tomographic reconstructions to be approximately 5 nm and 120-250 nm, respectively.

For lamella preparation following a 3D correlative workflow, the MAPS software provides 3-point correlation (based on features of grid squares) between the cryo-FLM and cryo-SEM images for 2D navigation in order to find squares for which the cryo-FLM data were acquired. About 10 microbeads were picked in the squares of interest and correlated between the cryo-FLM stacks (3D Gaussian plot to optimize geometry center) and the SEM images, as well as the FIB images (2D Gaussian plot to optimize geometry center) using 3DCT software (v2.2.2)[55]. After choosing the signal of interest in the confocal stacks, 3DCT provided the position as the center to place the parallel rectangular milling patterns above and below the center along the Y axis on FIB images, in order to retain the signal (region of interest) in the lamella. Milling is then performed as described above. After lamella generation, 3DCT was again used to correlate the cryo-FLM data with the SEM and FIB images to confirm that the signal of interest was retained in the lamella.

Cryo-electron tomography data collection

Cryo-electron tomography (ET) data of isolated nucleocapsids were collected on a Titan Krios microscope operated at 300 kV (Thermo Fisher Scientific) equipped with a field-emission gun, a Quantum post-column energy filter (Gatan) and a K2 direct detector camera (Gatan). Data were recorded in dose-fractionation mode using acquisition procedures in SerialEM software[56] v3.7.2. Prior

to the acquisition of tilt-series, montages of the grid squares were acquired at 3.106 nm/pixel to identify filamentous structures which were then confirmed as nucleocapsids at higher magnification. Tilt-series were collected for nucleocapsids using a dose symmetric scheme[57] in nano-probe mode, calibrated pixel size at the specimen level of 1.6938 Å, defocus range 2.5 to 3.5 µm, tilt increment 3° with constant dose of 2.5 $e^-/Å^2$ for all tilts, tilt range -60° to 60° starting from 0°, a total dose of ~102.5 $e^-/Å^2$. In total, twenty tomograms were acquired for the isolated nucleocapsids.

Cryo-ET data of FIB lamellae from cells at ~1 h of 0.5 mM As(III) stress for subtomogram averaging purpose were collected with the same Titan Krios microscope, except the pixel size used for lamella overviews of 2.284 nm/pixel and for tilt series of 3.3702 Å, defocus at 3.25 to 3.5 µm, increment 2° with constant dose of 2.5 $e^-/Å^2$ for all tilts, tilt range -60° to 54° starting from -12° (lamella pre-tilt angle), a total dose of ~145.0 $e^-/Å^2$. The AutoGrids with lamellae were carefully loaded with the lamella orientation (indent direction on custom-made AutoGrids) perpendicular to the tilt axis of the microscope for tilt series acquisition. For lamellae that were prepared following a 3D correlative approach, TEM overviews of lamella were overlaid with their SEM image that were already superimposed with the respective confocal oblique slice images (computed with MATLAB script), with the SerialEM registration points strategy. Two tomograms containing nucleocapsids were used for subsequent analyses.

Cryo-ET data of FIB lamellae from cells at ~2 h of 0.5 mM As(III), ~6 h of 30 µM As(III), or ~6 h of 1 mM As(V) stress conditions were collected on a different Titan Krios microscope equipped with a K3 direct detector camera (Gatan). Differences in settings are pixel size for lamella overview of 2.804 nm/pixel and for tilt series of 1.631 Å, defocus at 1.75 to 3.25 µm, increment 2° with constant dose of 2.6 $e^-/Å^2$ for all tilts, tilt range -60° to 60° (starting angle depending on pre-tilt angles of lamellae), a total dose of ~158.6 $e^-/Å^2$. In total, three tomograms containing nucleocapsids for ~2 h of 0.5 mM As(III), one tomogram for ~6 h of 30 µM As(III), and five tomograms for ~6 h of 1 mM As(V) were used for subsequent analyses.

In addition to tomograms described above, which were used for subtomogram averaging, cryo-ET data of nucleocapsids *in situ* at control and ~1 h of 0.5 mM As(III) stress were also collected with a Volta phase plate[58] (VPP, Thermo Fisher Scientific) for the purpose of better visualization. The operation of the VPP were carried out as described previously, applying a beam tilt of 10 mrad for autofocusing[59]. Pixel size for lamella map at 2.284 nm/pixel and for tilt series at 3.3702 Å, defocus at 2 to 3.75 µm, increment 2° with constant dose of 2.20 $e^-/Å^2$ for all tilts, tilt range -64° to 50° starting from -8°, and a total dose of ~127.6 $e^-/Å^2$ were used. In total, two tomograms containing nucleocapsids for control condition and one tomogram for ~1 h of 0.5 mM As(III) stress were used here for visualization.

Tomogram reconstruction

For processing of cryo-ET data of the isolated nucleocapsids, frames of the projection movies were imported to Warp software[60] (v1.0.9), for gain reference and beam-induced motion correction, as well as contrast transfer function (CTF) and astigmatism estimation. Prior to tomogram reconstruction in Warp, per-tilt averaged images were first imported to IMOD[61] (v 4.9.4) for tilt series alignment. Alignment of tilt-series images was performed with patch-tracking due to insufficient gold fiducials for tracking. Final alignment was done using the linear interpolation option in IMOD. Aligned images were initially 4 times binned to a pixel size of 6.7752 Å. Reconstruction of tilt series images was done in Warp at the same pixel size by importing the transformation files from IMOD to Warp. Deconvolved tomograms at the same binning were also reconstructed in Warp for segmentation purpose.

For processing of cryo-ET data of nucleocapsids *in situ* at ~1 h of 0.5 mM As(III) stress which were used for subtomogram averaging, the same procedures were followed except that initial tomograms were reconstructed by 4 times binning to a pixel size of 13.4808 Å. Neural network-based denoising was done in Warp at the same binning to generate tomograms for segmentation purpose.

For processing of cryo-ET data of nucleocapsids *in situ* at ~6 h of 30 µM As(III) stress or ~6 h of 1 mM As(V) stress which were used for subtomogram averaging, the same procedures were followed except that gain reference correction and motion correction were done in the SerialEM plugin, prior to Warp processing which started from per-tilt averaged images. Initial tomograms were reconstructed by 8 times binning to a pixel size of 13.048 Å. Neural network-based denoising was done in Warp at the same binning to generate tomograms for segmentation purpose.

For processing of cryo-ET data of nucleocapsids *in situ* at control and ~1 h of 0.5 mM As(III) stress for visualization purpose, frames of the projection movies were gain reference corrected and motion corrected in the SerialEM plugin. Tilt-series alignment and tomographic reconstructions were done in IMOD. Alignment of tilt-series images was performed with patch-tracking. Final alignment of the tilt-series images was performed using the linear interpolation option in IMOD without contrast transfer function correction. Aligned images were 4 times binned to a pixel size of 13.4808 Å. For tomographic reconstruction by back-projection, the radial filter options were left at their default values (cut off, 0.35; fall off, 0.05).

Filament tracing, volume fraction and persistence length analysis

Segmentation of *in situ* nucleocapsids was performed with the Fiber Tracing module in Amira software (v6.7 and v2019.4; Thermo Fisher Scientific), using the deconvolved or denoised tomograms. The approximate outer and inner diameters, helical pitch of nucleocapsids were measured from raw tomograms by averaging the values of multiple measurements, and used for as input for the tracing

parameters. The coordinates of the traced filaments were resampled with a MATLAB script to obtain equidistant points along the filament every 5.4 nm (4 pixels in datasets of 13.4808 Å/pixel). The approximate outer diameter of nucleocapsids as 21.30 nm was used for calculating the volumes of nucleocapsids per tomogram with the total lengths of nucleocapsid filaments calculated from tracing. Volume of regions per tomogram that contain nucleocapsids was obtained by manually segmenting areas where filaments were seen in Amira. The volume faction of nucleocapsids was then derived by dividing the volume of nucleocapsids to the total volume of regions containing nucleocapsids for individual tomograms. Tomograms with too few nucleocapsids (very small fractions of viral factories captured) were not used for volume fraction analysis.

Quantitative assessment of the morphology of nucleocapsid filaments was obtained by measurement of the persistence length (L_p), the distance for which a filament's direction persists before changing its course[62]. To determine its magnitude, we measured the difference between an angle θ_l between the tangents at points of distance l along the curved filament with respect to a fixed point on the filament l_0 with angle θ_0. Doing so for an ensemble of filaments in the tomographic volume, the correlation is determined by $\langle\cos(\theta_0 - \theta_l)\rangle = e^{-l/L_p}$. Mean length of filaments for each tomogram was determined to define the length range used for fitting of the slope. Persistence lengths of microtubules, actin, and lamina were determined *in situ* to be 12.07×10^3, 2.79×10^3, and 555.57 nm respectively in a previous report[54]. Nucleocapsids in our data are very flexible based on the persistence length comparison with these cytoskeletal filaments. Tomograms with too few nucleocapsids (very small fractions of viral factories captured) were not used for persistence length analysis.

Subtomogram averaging of isolated nucleocapsids

For subtomogram averaging of the isolated nucleocapsids, nucleocapsids were first traced in Dynamo package[63] (v1.1.401) with the 4 times binned tomograms. In the Dynamo model generation interface, extremal points of relatively straight segments along each nucleocapsid were manually selected to define the central line "backbone". Bent regions were discarded. Directionality of individual nucleocapsids were visually inspected and considered when selecting extremal points. Successive orthogonal sections along the nucleocapsid backbone were then generated such that central points of these sections were manually adjusted to define series of ordered points composing the refined backbone. After that, the Dynamo filament model with torsion type was used for generation of subtomograms (called "subunits" in Dynamo). The torsion effect in this model refers to the fact that the x direction of two subsequent subtomograms can be chosen to vary a fixed angle. Two parameters subunits_dz and subunits_dphi were set as 8 pixels (5.4 nm) and 30°, considering the helical pitch and nucleoprotein subunits per turn roughly measured/counted from tomograms, as well as for reducing the effect of missing wedge in subtomogram averaging[64]. Subtomograms (4 times binned, box size of 64^3 pixels) were cropped using Dynamo with the model-defined positions and initial Euler angles were

generated relative to filament axes with extra in-plane rotations derived from torsion angles (Extended Data Fig. 6a).

Reference-free subtomogram averaging/refinement was performed using Dynamo, adapted TOM[65] and AV3[66] (TOM/AV3) software toolboxes and derived MATLAB scripts, RELION[67] (v3.0 and v3.1), Warp and M[68] (v1.0.9). Initial reference was generated by averaging subtomograms (4 times binned) from a single long nucleocapsid without alignment. A cylindrical mask was generated in Dynamo according to the initial average, and used as alignment mask. Other masks were left as default. Subtomograms from the single long nucleocapsid were iteratively aligned against the initial reference in Dynamo, performing Euler angles and Cartesian shifts search. The resulting average of the single long nucleocapsid was used to align all subtomograms extracted from 20 tomograms, with the first two Euler angles restrained to not allow flipping during angular search. After the first round of rough alignment with a low-pass filter of ~35 Å, the resulting average showed polarity. To determine the directionality of individual nucleocapsid, averages of subtomograms belonging to individual nucleocapsid with refined positions and angles were visually inspected. Subtomograms of nucleocapsids with opposite directionality to the initial long nucleocapsid were flipped by modifying their Euler angles. After directionality check, rounds of iterative alignment were done until convergence. The refined coordinates of subtomograms were used for reconstructing 2 times binned subtomograms in Warp.

The subtomograms were then split into odd and even sets at 2 times binning for alignment using TOM/AV3 toolboxes. The odd and even sets were aligned independently using the average of each set as initial reference. Low-pass filter and angular search range/sampling parameters were adjusted based on the Fourier Shell correlation (FSC) plots after each round of alignment until convergence. After that, distance-based cleanup of subtomograms was done with MATLAB scripts to remove particles that were too close due to shift during alignment and the ones with higher constrained cross correlation (CCC) values were kept. The refined coordinates of subtomograms were used for reconstructing unbinned subtomograms (box size of 256^3) with per-particle CTF models in Warp.

Unbinned subtomograms were averaged with refined Euler angles from TOM/AV3 alignment and intensity-inverted to generate initial reference for RELION 3D auto-refinement. Then, standard 3D auto-refinement was performed without symmetry, with a soft-edged sphere-multiplied cylindrical mask which was generated using relion_helix_toolbox (outer diameter 220 Å, sphere percentage 0.55). A 30 Å lowpass-filtered map generated from TOM/AV3 alignment was used as an initial reference. 1,209 subtomograms led to a 10 Å map with no symmetry applied. Helical parameters were estimated with relion_helix_toolbox, resulting in an average helical rise of 4.46 Å and helical twist of -27.08° (left-handed, ~13.3 subunits per turn). Next, helical symmetry was imposed in RELION 3D auto-

refinement with local symmetry search, resulting in the refined average helical rise of 4.16 Å and helical twist of -27.16°. After RELION classification with helical symmetry imposed, two classes of distinct helical parameters were separated: the majority class (77.7%, 4.21Å/-27.17°, map at 6.5 Å after auto-refinement) and the minority class (21.3%, 3.51Å/-26.9°, map at 7.3 Å after auto-refinement).

Positions and orientations of RELION symmetry-expanded subtomograms of the majority class were next used for refining tilt series alignment and CTF models in M software[18]. After resolution convergence was reached in M (4.8 Å), new non-symmetry expanded subtomograms were reconstructed in Warp. One more round of RELION 3D auto-refinement imposing helical symmetry (which remained the same after M refinement) resulted in a final map of 4.5 Å for the majority class within the reconstruction mask. The minority class was refined in a newer version of M which allowed to set helical symmetry parameters. After resolution convergence was reached in M, subtomograms were again reconstructed in Warp. One more round of RELION 3D auto-refinement imposing helical symmetry (remaining the same after M refinement) resulted in a final map of 6.3 Å for the minority class within the reconstruction mask with the 0.143 criterion.

Maps used for structural analysis were obtained by filtering to the estimated resolution using the RELION Post-processing module with the same sphere-multiplied cylindrical mask. Visualization of density maps were done with UCSF Chimera[69] (v1.13.1)/ChimeraX[70] (v1.1.1). FSC plots were obtained with the RELION Post-processing module using the same sphere-multiplied cylindrical mask. Local resolution estimation was also done in RELION with the Local resolution module providing the B-factors obtained from post-processing jobs and the masks. Local resolution maps were rendered with Chimera.

Subtomogram averaging of straight nucleocapsids *in situ*

For subtomogram averaging of the relatively straight nucleocapsids *in situ* (at ~6 h of 30 µM As(III) and ~6 h of 1 mM As(V) stress), the coordinates of the traced filaments were resampled with a MATLAB script to obtain equidistant points along the filament at every 5.2 nm (4 pixels of 8 times binned data, 13.4808 Å/pixel) and with a torsion angle (30°) assigned in similar way as for the isolated nucleocapsids (Extended Data Fig. 7d). These equidistant points were used as center points for extraction of subtomograms (box size of 32^3) with Dynamo crop function. Alignment of 8 times binned subtomograms were done with Dynamo. Alignment started with the longest nucleocapsid in one tomogram exhibiting the longest persistence length. As described above, initial average was generated and used as reference for alignment of subtomograms in this longest nucleocapsid. The resulting average was used for alignment of subtomograms from four long nucleocapsids in this tomogram. To determine the directionality of the other three nucleocapsids, averages of subtomograms belonging to individual nucleocapsid with refined positions and angles were visually inspected. Subtomograms of

nucleocapsids with opposite directionality to the longest nucleocapsid were flipped by modifying their Euler angles. After directionality check, alignment was re-done with subtomograms from these four nucleocapsids. The resulting average was next used to align all subtomograms in six tomograms for one round of angular and translational search. Directionality check was done for individual nucleocapsid as described above. Only nucleocapsids showing clear directionality amongst those longer than 100 nm were kept for further processing. Subtomograms of nucleocapsids with opposite directionality to the longest nucleocapsid were flipped by modifying their Euler angles. Next, two more rounds of iterative alignment were done until convergence. Similarly, distance- and CCC-based cleaning of subtomograms was done with MATLAB scripts. The refined coordinates of subtomograms were used for reconstructing 4 times binned subtomograms in Warp.

The 4 times binned subtomograms were then aligned using TOM/AV3 toolboxes. After three rounds of iterative alignment, distance- and CCC-based cleanup of subtomograms was done. The refined coordinates of subtomograms were used for reconstructing two times binned subtomograms (box size of 128^3) with per-particle CTF models in Warp.

The 2 times binned subtomograms were used for RELION 3D auto-refinement, following similar procedures as described for the isolated nucleocapsids. 2,178 subtomograms led to a 22 Å map with no symmetry applied. Helical parameters were estimated with relion_helix_toolbox and helical symmetry was imposed in RELION 3D auto-refinement with local symmetry search, resulting in the refined average helical rise of 4.24 Å and helical twist of -27.19°, and improved map resolution to 8.9 Å. RELION classification with helical symmetry imposed resulted in classes with very similar helical parameters, and were thus combined for further refinement. Positions and orientations of RELION helical symmetry-expanded subtomograms were next used for refining tilt series alignment and CTF models in M software. After resolution convergence was reached in M at 2 times binning, new non-symmetry expanded subtomograms were reconstructed in Warp. One more round of RELION 3D auto-refinement imposing helical symmetry resulted in a map of improved resolution at 7.2 Å and of the same helical parameters as the majority class in subtomogram averaging of isolated nucleocapsids (rise as 4.21Å and twist as -27.17°).

Unbinned subtomograms (box size of 256^3) were then reconstructed in Warp at refined positions and subjected to RELION 3D auto-refinement. This step of 3D auto-refinement did not improve the resolution and classification resulted in very minor difference in helical parameters. The map was further refined in M which allowed to set helical symmetry parameters. After resolution convergence was reached in M, subtomograms were again reconstructed in Warp. One more round of RELION 3D auto-refinement imposing helical symmetry (remaining the same after M refinement) resulted in a final map of 6.5 Å within the reconstruction mask with the 0.143 criterion.

The map used for structural analysis was obtained by filtering to the estimated resolution using the RELION Post-processing module with the sphere-multiplied cylindrical mask.

Subtomogram averaging of curved nucleocapsids *in situ*

For subtomogram averaging of the curved nucleocapsids *in situ* (at ~1 h of 0.5 mM As(III) stress), the coordinates of the traced nucleocapsids (done in Amira) were over-sampled with a MATLAB script to obtain uniformly distributed positions on the surfaces of nucleocapsid at every 2.7 nm (4 pixels of 2 times binned data), with initial Euler angles assigned at each surface position, and the new Z axis assigned perpendicular to the nucleocapsid axis (Extended Data Fig. 7a). These surface positions were used as extraction points for subtomogram reconstruction in Warp.

Alignment of 2 times binned subtomograms (box size of 36^3) was done with TOM/AV3 toolboxes. The initial average was generated by aligning and averaging subtomograms of the longest nucleocapsid in a tomogram acquired with VPP, which has better contrast (signal-to-noise ratio) at low spatial frequency range. The VPP-average was used for alignment of subtomograms of all nucleocapsids in the two tomograms acquired without VPP. After 5 iterations of initial alignment, nucleocapsid directionality was checked by visual inspection of subtomogram averages of individual nucleocapsid. However, determination of the directionality was difficult due to poor signal-to-noise ratio of individual average. Thus, sampling was re-done at equidistant points along the central line of nucleocapsids and subtomograms were extracted for generation of averages of individual nucleocapsid, only for determination of directionality. Nucleocapsids showing clear directionality amongst those longer than ~130 nm were kept for further processing. Subtomograms (oversampled) of nucleocapsids with opposite directionality to the VPP-average were flipped by modifying their Euler angles. Next, the VPP-average was again used to align the remaining 27,464 subtomograms (oversampled) until convergence. After that, distance- and CCC-based cleaning of clashing subtomograms was done with MATLAB scripts, with 4 pixels (2.7 nm) as a threshold. The refined coordinates of the 10,702 remaining subtomograms were used for reconstruction of subtomograms at 2 times binning in Warp with the same box size.

The re-extracted 2 times binned subtomograms were used for RELION 3D Classification using the average converted from TOM/AV3 alignment as a reference (filtered to 40 Å). Four classes were generated and one class (2882 particles) was discarded due to poor signal to noise ratio. The other three classes (2452, 2726, 2642 particles each) were separately refined, all resulting in maps of ~30 Å in resolution. Further refinement using smaller masks did not improve maps, but resulted in too little content to be compared with higher resolution maps of isolated nucleocapsids. The maps used for

structural analysis were obtained by filtering to the estimated resolution using the RELION Post-processing module with the refinement mask.

Model building

To build a pseudo-atomic model for the majority class of the isolated nucleocapsids resolved to 4.5 Å, an initial model of MuV-N was generated with the homolog N protein of parainfluenza virus 5 (PIV5) (PDB: 4XJN) as a template using I-TASSER[71]. The initial model was first fitted into the map of the majority class as a rigid-body, together with six RNA bases from the PIV5 model using Chimera. Only the core part of N (amino acid 3-405) was used for model building because the density for C-terminal flexible region was missing. Then, the combined model of N and RNA was subjected to one round of automated refinement using Phenix[72] (v 1.18-3845) with minimization_global, local_grid_search, simulated_annealing, and ADP strategies, and restraining rotamers, Ramachandran and secondary structures. Next, three copies of the refined N and RNA were generated and rigid-body docked to EM density corresponding to the subunit at N_{i+1} position with respect to the original one (N_i). Two additional subunits were docked into the upper turn in order to take interaction interfaces into account. After that, the tetramer model was per-residue manually refined in *Coot*[73] (v0.9) using Peptide and Ramachandran restraints, with attention on the first monomer and molecular interfaces. Regions poorly fitted were deleted and re-built. N- and C-termini were checked and more residues added in case densities were seen. The RNA bases were modeled as poly-Uracils considering the averaging effect. Density modification strategy in Phenix.ResolveCryoEM was used to generate a map for aiding model inspection in *Coot*, but automated refinement and validation were done against the original map. The refined model of the first monomer was again copied and rigid body docked into the density map for a second round of automated refinement with Refine NCS operators on. Additional rounds of manual inspection and automated refinement were performed until convergence and Refine NCS operators was not used in the last round. The real-space cross-correlation of each residue to the map was calculated and plotted in order to evaluate the quality of the model (Extended Data Fig. 6d). The masked FSC between the original map and a simulated map calculated from the tetramer model at 0.5 cutoff gave a resolution estimate of 4.5 Å, similar to the estimate from the half map FSC 0.143 cutoff. MolProbity statistics were computed to ensure proper stereochemistry. Monomer of the model was used for rigid-body fitting into the map of straight nucleocapsids *in situ* (6.5 Å) with Chimera.

Methods references

43 Poser, I. *et al.* BAC TransgeneOmics: a high-throughput method for exploration of protein function in mammals. *Nat Methods* **5**, 409-415, doi:10.1038/nmeth.1199 (2008).

44 Fujii, N. *et al.* Suppression of interferon-induced oligo-2',5'-adenylate synthetase induction in persistent infection. *J Gen Virol* **71 (Pt 12)**, 3071-3074, doi:10.1099/0022-1317-71-12-3071 (1990).

45 Schindelin, J. *et al.* Fiji: an open-source platform for biological-image analysis. *Nat Methods* **9**, 676-682, doi:10.1038/nmeth.2019 (2012).

46 Mateus, A. *et al.* The functional proteome landscape of Escherichia coli. *Nature* **588**, 473-478, doi:10.1038/s41586-020-3002-5 (2020).

47 Hughes, C. S. *et al.* Single-pot, solid-phase-enhanced sample preparation for proteomics experiments. *Nat Protoc* **14**, 68-85, doi:10.1038/s41596-018-0082-x (2019).

48 Huber, W., von Heydebreck, A., Sultmann, H., Poustka, A. & Vingron, M. Variance stabilization applied to microarray data calibration and to the quantification of differential expression. *Bioinformatics* **18 Suppl 1**, S96-104, doi:10.1093/bioinformatics/18.suppl_1.s96 (2002).

49 Ritchie, M. E. *et al.* limma powers differential expression analyses for RNA-sequencing and microarray studies. *Nucleic Acids Res* **43**, e47, doi:10.1093/nar/gkv007 (2015).

50 Yu, G., Wang, L. G., Han, Y. & He, Q. Y. clusterProfiler: an R package for comparing biological themes among gene clusters. *OMICS* **16**, 284-287, doi:10.1089/omi.2011.0118 (2012).

51 Rigort, A. *et al.* Micromachining tools and correlative approaches for cellular cryo-electron tomography. *J Struct Biol* **172**, 169-179, doi:10.1016/j.jsb.2010.02.011 (2010).

52 Allegretti, M. *et al.* In-cell architecture of the nuclear pore and snapshots of its turnover. *Nature* **586**, 796-800, doi:10.1038/s41586-020-2670-5 (2020).

53 Schaffer, M. *et al.* Optimized cryo-focused ion beam sample preparation aimed at in situ structural studies of membrane proteins. *J Struct Biol* **197**, 73-82, doi:10.1016/j.jsb.2016.07.010 (2017).

54 Mahamid, J. *et al.* Visualizing the molecular sociology at the HeLa cell nuclear periphery. *Science* **351**, 969-972, doi:10.1126/science.aad8857 (2016).

55 Arnold, J. *et al.* Site-Specific Cryo-focused Ion Beam Sample Preparation Guided by 3D Correlative Microscopy. *Biophys J* **110**, 860-869, doi:10.1016/j.bpj.2015.10.053 (2016).

56 Mastronarde, D. N. Automated electron microscope tomography using robust prediction of specimen movements. *J Struct Biol* **152**, 36-51, doi:10.1016/j.jsb.2005.07.007 (2005).

57 Hagen, W. J. H., Wan, W. & Briggs, J. A. G. Implementation of a cryo-electron tomography tilt-scheme optimized for high resolution subtomogram averaging. *J Struct Biol* **197**, 191-198, doi:10.1016/j.jsb.2016.06.007 (2017).

58 Danev, R., Buijsse, B., Khoshouei, M., Plitzko, J. M. & Baumeister, W. Volta potential phase plate for in-focus phase contrast transmission electron microscopy. *Proceedings of the National Academy of Sciences of the United States of America* **111**, 15635-15640, doi:10.1073/pnas.1418377111 (2014).

59 Fukuda, Y., Laugks, U., Lucic, V., Baumeister, W. & Danev, R. Electron cryotomography of vitrified cells with a Volta phase plate. *J Struct Biol* **190**, 143-154, doi:10.1016/j.jsb.2015.03.004 (2015).

60 Tegunov, D. & Cramer, P. Real-time cryo-electron microscopy data preprocessing with Warp. *Nat Methods* **16**, 1146-1152, doi:10.1038/s41592-019-0580-y (2019).

61 Kremer, J. R., Mastronarde, D. N. & McIntosh, J. R. Computer visualization of three-dimensional image data using IMOD. *J Struct Biol* **116**, 71-76, doi:10.1006/jsbi.1996.0013 (1996).

62 Nagashima, H. & Asakura, S. Dark-field light microscopic study of the flexibility of F-actin complexes. *J Mol Biol* **136**, 169-182, doi:10.1016/0022-2836(80)90311-3 (1980).

63 Castano-Diez, D., Kudryashev, M., Arheit, M. & Stahlberg, H. Dynamo: a flexible, user-friendly development tool for subtomogram averaging of cryo-EM data in high-performance computing environments. *J Struct Biol* **178**, 139-151, doi:10.1016/j.jsb.2011.12.017 (2012).

64 Wan, W. & Briggs, J. A. Cryo-Electron Tomography and Subtomogram Averaging. *Methods in enzymology* **579**, 329-367, doi:10.1016/bs.mie.2016.04.014 (2016).

65 Nickell, S. *et al.* TOM software toolbox: acquisition and analysis for electron tomography. *J Struct Biol* **149**, 227-234, doi:10.1016/j.jsb.2004.10.006 (2005).

66 Forster, F. & Hegerl, R. Structure determination in situ by averaging of tomograms. *Methods Cell Biol* **79**, 741-767, doi:10.1016/S0091-679X(06)79029-X (2007).

67 Zivanov, J. *et al.* New tools for automated high-resolution cryo-EM structure determination in RELION-3. *Elife* **7**, doi:10.7554/eLife.42166 (2018).

68 Tegunov, D., Xue, L., Dienemann, C., Cramer, P. & Mahamid, J. Multi-particle cryo-EM refinement with M visualizes ribosome-antibiotic complex at 3.5 A in cells. *Nat Methods* **18**, 186-193, doi:10.1038/s41592-020-01054-7 (2021).

69 Pettersen, E. F. *et al.* UCSF Chimera--a visualization system for exploratory research and analysis. *J Comput Chem* **25**, 1605-1612, doi:10.1002/jcc.20084 (2004).

70 Pettersen, E. F. *et al.* UCSF ChimeraX: Structure visualization for researchers, educators, and developers. *Protein Sci* **30**, 70-82, doi:10.1002/pro.3943 (2021).

71 Roy, A., Kucukural, A. & Zhang, Y. I-TASSER: a unified platform for automated protein structure and function prediction. *Nat Protoc* **5**, 725-738, doi:10.1038/nprot.2010.5 (2010).

72 Liebschner, D. *et al.* Macromolecular structure determination using X-rays, neutrons and electrons: recent developments in Phenix. *Acta Crystallogr D Struct Biol* **75**, 861-877, doi:10.1107/S2059798319011471 (2019).

73 Emsley, P., Lohkamp, B., Scott, W. G. & Cowtan, K. Features and development of Coot. *Acta Crystallogr D Biol Crystallogr* **66**, 486-501, doi:10.1107/S0907444910007493 (2010).